1   **Brittle Deformation of Carbonated Peridotite – Insights from Listvenites of**

2   **the Samail Ophiolite (Oman Drilling Project Hole BT1B)**

Manuel D. Menzel[1*], Janos L. Urai[1,2], Juan Carlos de Obeso[3], Alissa Kotowski[4^], Craig E. Manning[5], Peter B. Kelemen[3], Michael Kettermann[6], Ana P. Jesus[2#], Yumiko Harigane[7], and the Oman Drilling Project Phase 1 Science Team

[1]*Institute of Structural Geology, Tectonics and Geomechanics, RWTH Aachen University, Germany*

[2]*German University of Technology GUtech, Muscat, Oman*

[3]*Lamont–Doherty Earth Observatory, Columbia University, USA*

[4]*Department of Geological Sciences, Jackson School of Geosciences, University of Texas at Austin, Austin, TX USA*

[5]*University of California Los Angeles, USA*

[6]*Department of Geodynamics and Sedimentology, University of Vienna, Austria*

[7]*Institute of Geology and Geoinformation, Geological survey of Japan, National Institute of Advanced Industrial Science and Technology, Tsukuba 305-8567, Japan*

^ *Now at Department of Earth and Planetary Sciences, McGill University, Montreal, Quebec, Canada*

now at Instituto Dom Luiz (IDL), Faculdade de Ciências, Universidade de Lisboa, Lisboa, Portugal

*Corresponding author email: manuel.menzel@emr.rwth-aachen.de

3

4   **Key Points:**

5   • Abundant cataclasites overprint previously formed listvenite in the Oman Drilling
6   Hole BT1B.

7   • Cataclasis was related to fluid flow, which caused Mg loss and/or Si enrichment, and
8   local redistribution of Cr.

9   • The multistage tectonic overprint after peridotite carbonation in the Oman ophiolite
10   should be excluded when analysing early structures.

11 **Abstract**

12 Hole BT1B of the Oman Drilling Project provides a continuous sampling from listvenite into
13 the metamorphic sole that preserves the deformation, hydration and carbonation processes of
14 oceanic mantle peridotite at the base of the Samail ophiolite, Oman. We present evidence of
15 multistage brittle deformation in listvenites and serpentinites based on field observations,
16 visual core logging and petrography. About 10 vol% of listvenite and serpentinite in Hole
17 BT1B is composed of cataclasite bands. Cataclasites contain lithic clasts of listvenite with
18 spheroidal, zoned magnesite and quartz, and fragments of chalcedony-carbonate veins that
19 elsewhere crosscut listvenite — showing that cataclasis post-dates listvenite formation.
20 Locally the cataclasites are reworked and cut by thin, sharp faults, pointing to repeated
21 reactivation of brittle structures. SEM-EDS mapping shows that cataclasis was related to
22 silica cementation and/or dissolution of carbonate. Dolomite veins crosscut cataclasites and
23 breccias, suggesting that part of the Ca gain in BT1B is related to late fluids after listvenite
24 formation. These results indicate a multistage tectonic overprint after peridotite carbonation
25 and listvenite formation, which may be related to the tectonic history of the deformed
26 continental margin under the ophiolite. These relatively late brittle structures should be
27 excluded when trying to understand the carbonation of peridotite to listvenite.

28 *Keywords: Oman Drilling Project, peridotite carbonation, ophiolite obduction, cataclasite*

29

1. Introduction

30

31   The interaction of mantle rocks with aqueous fluids causes large amounts of volatiles to be
32   stored in altered peridotite due to hydration (serpentinization) and carbonation reactions of
33   olivine and pyroxene. These reactions are particular in that they produce very volatile-rich
34   alteration products (up to 15 wt% H_2O or 35 wt% CO_2 in fully hydrated or carbonated
35   peridotite, respectively), have comparatively fast reaction rates, and can pervasively transform
36   large volumes of rock (Kelemen et al., 2011). Therefore, the alteration of Mg-bearing silicates
37   in peridotite can have a substantial impact on the global geochemical cycling of volatiles (Alt
38   et al., 2013; Beinlich et al., 2018). In particular, peridotites in the cold part of the mantle
39   wedge of subduction zones may take up large amounts of water and carbon during
40   serpentinization and carbonation reactions caused by C-bearing, aqueous subduction fluids
41   derived from the slab (Hyndman and Peacock, 2003; Kelemen and Manning, 2015). The
42   reaction characteristics of olivine and pyroxene alteration further make exposures of
43   peridotites in ophiolites a promising target for strategies of carbon sequestration by mineral
44   carbonation (Kelemen et al., 2018; Kelemen & Matter, 2008; Paukert et al., 2012).

45   In the extreme, the interaction of peridotite with C-bearing fluid produces listvenite, a rock
46   where all Mg-bearing silicates are replaced by carbonate and quartz, and relict chromian
47   spinel is partly transformed into chromian mica (fuchsite-muscovite solid solutions) (Halls
48   and Zhao, 1995). Listvenites often are associated with talc-carbonate assemblages (soapstone)
49   and carbonate-bearing serpentinites, which form at different fluid/rock ratios during the
50   interaction of peridotite with C-bearing aqueous fluids (Beinlich et al., 2012; Hansen et al.,
51   2005; Menzel et al., 2018). Because serpentinized peridotites have low Ca contents,
52   carbonates in listvenites are typically magnesite and minor dolomite. C-bearing fluids are
53   commonly interpreted to be derived from underlying carbonate-bearing metasediment.
54   Locally, listvenites can be associated with birbirite – silicified serpentinite consisting mostly
55   of quartz with only minor carbonate and relict Cr-spinel (Akbulut et al., 2006; Lacinska &
56   Styles, 2013; Nasir et al, 2007; Stanger, 1985) – or magnesite-fuchsite rocks that contain only
57   traces of quartz (Menzel et al., 2018). Thermodynamic models suggest that both birbirites and
58   magnesite-rich rocks can be the result of extended fluid-rock interaction to high water/rock
59   ratios after listvenite formation at different temperatures (Klein and Garrido, 2011).

60   A very interesting and controversial aspect of the hydration and carbonation of peridotite is
61   how these reactions can go to completion. Because solid mass is increased by addition of
62   H_2O, CO_2, and the hydrated and carbonated solid products have lower densities than the solid
63   reactants, reactions increase the solid volume. Fluid–rock reactions that increase the solid
64   volume may fill porosity, reduce permeability, and produce reaction rims to stop the reaction
65   (Andreani et al., 2009; Farough et al., 2016; Godard et al., 2013; Oelkers et al., 2018; van
66   Noort et al., 2017). Accordingly, observations in experiments of carbonation of natural
67   peridotite by several groups (Andreani et al. 2009; Godard et al. 2013; Hövelmann et al.,
68   2013; van Noort et al. 2017) showed decreasing permeability, suggesting that the carbonation
69   reaction was self-limiting in these experiments. However, in nature, replacement of peridotite
70   by carbonates can proceed to completion, as shown by listvenites. A key to how this process
71   goes to completion may be hierarchical fracture networks, where the crystallization pressure
72   creates local gradients in differential stress and drives fractures, which in turn increase
73   permeability and reactive surface area (e.g., Malthe-Sørenssen et al., 2006; O'Hanley, 1992;
74   Rudge et al., 2010; Ulven et al., 2014), as experimentally demonstrated for hydration of
75   periclase (Zheng et al., 2018). On a larger scale, volume change may also cause differential
76   stress and fracture, as proposed for olivine hydration by Macdonald and Fyfe (1985).

77 Alternatively, anisotropic far field stress in tectonic deformation can lead to dilatancy and
78 allow the reaction to go to completion.

79 A review by Kelemen and Hirth (2012) suggests that the crystallization pressure during
80 carbonation of peridotite can be very large, and argues that this process can lead to a positive
81 feedback due to cracking, allowing the reaction to go to completion. Phase field models
82 suggest a positive feedback between reaction driven cracking and the local rate of peridotite
83 hydration in hierarchical vein networks (Evans et al., 2020), a process that may also apply to
84 carbonation reactions. Zhu et al. (2016) conducted a mineral carbonation experiment on
85 olivine using synchrotron X-ray micro-tomography, which showed polygonal cracks
86 propagating into the interior of the olivine aggregate. They infer that non-uniform volume
87 expansion induced by the reactions generates polygonal cracking of the surfaces. In addition,
88 the reaction products may be micro-to nano-porous, providing fluid pathways through the
89 matrix, which may cause microstructural maintenance and enhancement of permeability via
90 combined dissolution and precipitation processes (Malvoisin et al., 2020; Peuble et al., 2015;
91 Tutolo et al., 2016). Studies propose that that dissolution etch pits along dislocations in
92 olivine are preferentially filled with reaction products and form the nucleus for microcracks
93 (Klein et al., 2015; Peuble et al., 2018; Plümper et al., 2012; Xing et al., 2018).

94 Brittle deformation may therefore play a key role in increasing the reactive surface area and
95 maintaining or enhancing permeability. Accordingly, some engineering approaches to carbon
96 sequestration by olivine carbonation achieve higher reaction rates by powdering of the
97 reactant material (e.g. Li and Hitch, 2018, and references therein). However, in the absence of
98 continued deformation during reaction, permeability reduction and deactivating silica reaction
99 rims often prevail and inhibit complete carbonation (van Noort et al., 2017). Compaction and
100 triaxial deformation experiments suggest mechanically enhanced dissolution rates during
101 hydration and carbonation of olivine (Lisabeth et al., 2017). In natural reservoir and crustal
102 conditions, mechanically enhanced reaction rates are likely to occur in brittle fault zones that
103 are characterized by high permeability and renewal of reactive surfaces due to faulting and
104 cataclasis. Listvenites are indeed often related to major thrust faults and show evidence of
105 brittle deformation such as tectonic breccias and veins (Escayola et al., 2009; Menzel et al.,
106 2018; Qiu and Zhu, 2018).

107 The Samail ophiolite in Oman includes large surface exposures of variably hydrated and
108 carbonated mantle rocks – an ideal place to study the interaction between rock deformation
109 and peridotite alteration. Listvenites occur along the basal thrust of the ophiolite in the Samail
110 massif (Nasir et al., 2007; Wilde et al., 2002). Previous field, geochemical and microstructural
111 studies of the Oman listvenites (Falk and Kelemen, 2015; Kelemen et al., 2011; Nasir et al.,
112 2007; Rajendran et al., 2013; Stanger 1985) did not address how the transformation of
113 peridotite to listvenite could proceed at a large scale. In parts this is due to the outcrop
114 conditions with thick weathering crusts and abundant fracturing, which also hindered a
115 systematic study of deformation structures. Hole BT1B of the Oman Drilling Project was
116 drilled for this reason, to acquire a fresh core from a continuous section from listvenite into
117 the metamorphic sole that would allow systematic (micro)structural and geochemical logging
118 of the carbonation reaction processes. The tabular nature of listvenite bands in partially
119 serpentinized peridotite at Oman Drilling Site BT1, parallel to the gently dipping basal fault
120 of the ophiolite, suggests that large scale, imbricate faults may have played a role in guiding
121 the CO_2-bearing fluids that formed listvenite.

122   Here we present evidence of multistage brittle deformation in listvenites and serpentinites
123   based on field observations, visual core inspection and petrography, using the unique sample
124   set from Hole BT1B. The aim of this contribution is to study whether widespread cataclasites
125   in the Oman listvenites are coeval with carbonation and are examples of mechanically
126   enhanced reaction rates, or whether they post-date listvenite formation. In order to evaluate
127   the possibility of post-obduction tectonic overprint for cataclasite formation in listvenite, we
128   further compare the cataclasite and fault microstructures and conditions with post-
129   emplacement structures in the underlying carbonate-bearing units.

130   ## 2. Geological setting

131   ### 2.1. Tectonic evolution of the Oman mountains

132   The Samail ophiolite (Fig. 1a) exposes a relatively intact sequence of obducted oceanic crust
133   (4 – 8 km thick; Nicolas et al., 1996) and mantle (9 – 12 km thick in the Wadi Tayin massif;
134   Hanghøj et al. 2010; Hopson et al., 1981) formed during the Cenomanian (96.5 – 95.5 Ma;
135   Rioux et al. (2013)) at a fast-spreading mid-ocean ridge or a supra-subduction zone spreading
136   center (Coleman, 1981; Glennie et al., 1974; Searle and Cox, 1999). Intra-oceanic subduction
137   of oceanic crust and sediment slices led to the formation of a high grade metamorphic sole
138   beginning at about the same time as ophiolite formation (Hacker et al., 1996; Rioux et al.
139   2013) or up to 10 Ma earlier (Guilmette et al. 2018; Soret et al., 2020). The sole records
140   amphibolite to granulite facies peak metamorphic conditions (530 – 850 °C, 0.5 – 1.0 GPa)
141   and was exhumed along with peridotite at the basal thrust during ophiolite obduction (Cowan
142   et al., 2014; Ghent and Stout, 1981; Hacker and Mosenfelder, 1996; Soret et al., 2017). The
143   emplacement of the Samail ophiolite occurred by obduction onto allochthonous distal
144   sediments (the Hawasina formation) in the first, intra-oceanic subduction stage, and
145   subsequent top-to-S thrusting of both ophiolitic and allochthonous sediment nappes onto the
146   thick autochthonous sediments of the Mesozoic passive margin of the Arabian plate (e.g.
147   Searle and Cox, 1999). The Jebel Akhdar and Saih Hatat anticlinoria, exposed in peaks up to
148   3000 m high in the Al Hajar mountain range, form large-scale tectonic windows that permit
149   the reconstruction of post-obduction tectonics that affected the continental carbonate platform
150   due to the emplacement of the Hawasina and ophiolite nappes (Fig. 1a). Partial subduction
151   and burial of the passive margin below the ophiolite nappe caused heating to different peak
152   metamorphic conditions from 450 – 550 °C, 2.0 – 2.4 GPa in eclogite of the deepest As Sifah
153   complex NE of the Saih Hatat dome, to 280 – 360 °C, < 0.5 – 1.0 GPa in the NW Saih Hatat
154   (Agard et al., 2010; Miller et al., 1999; Saddiqi et al., 2006; Searle et al., 1994), and 300 – 360
155   °C, 0.28 – 0.34 GPa (lithostatic pressure) recorded in veins in carbonates of the Jebel Akhdar
156   dome (Grobe et al., 2019). The burial caused fluid overpressure, and generation and migration
157   of hydrocarbons, but little deformation in the carbonate platform (Grobe et al., 2016). This
158   was followed by top-to-NNE ductile shear zones (Al-Wardi and Butler, 2007; Grobe et al.,
159   2016), the deformation of earlier veins, and the formation of mylonitic marbles in the early
160   Campanian (~80 – 60 Ma) (Grobe et al., 2018). Normal and oblique-slip faults with horst-
161   graben structures formed during Campanian to Maastrichtian times, after ophiolite obduction,
162   with extension and dome exhumation (Grobe et al., 2018) accompanied by sub-aerial erosion
163   of the ophiolite followed by deposition of shallow marine carbonates (e.g. Nolan et al., 1990).
164   This was followed by NE-SW shortening in the Miocene to Pliocene during large-scale
165   folding of the Jebel Akhdar and Saih Hatat domes, which tilted the earlier structures (Gomez-
166   Rivas et al., 2014; Grobe et al., 2018). Widespread strike-slip faults postdate the large-scale

167 folding (Gomez-Rivas et al., 2014; Grobe et al., 2018; Virgo et al., 2013). At the Northern
168 flank of Jebel Akhdar, final exhumation of the core of the anticlinorium occurred along
169 detachments (Grobe et al., 2018).

170
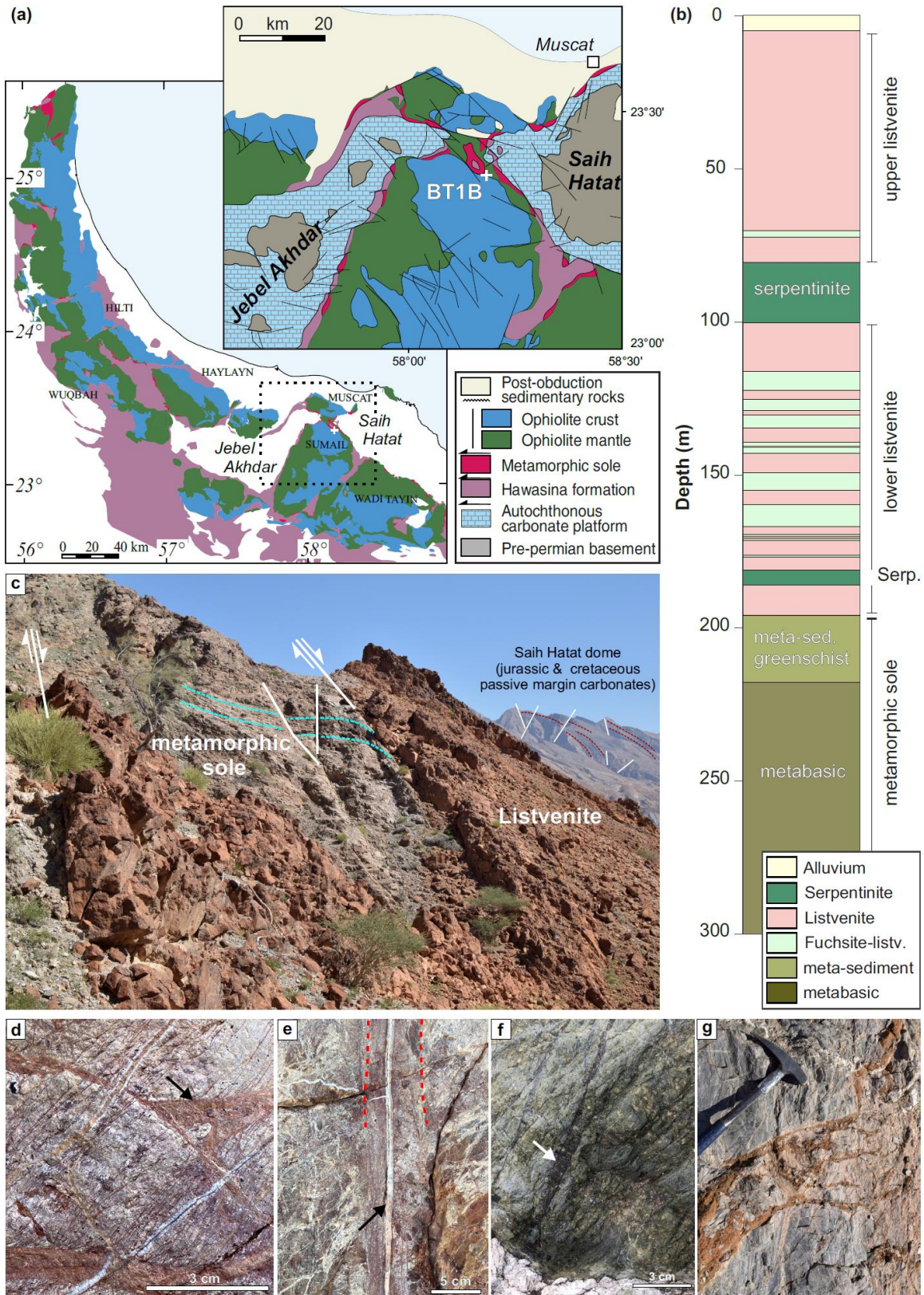
Fig. 1 (a) Lithological column of Hole BT1B; (b) Simplified geological overview map of Northern Oman (after Nicolas & Boudier, 1995), and geology of the northern Samail massif (after Béchennec et al., 1992); (c) field view of the contact between listvenite and greenschists of the metamorphic sole looking east, with the Saih Hatat dome in the background; (d) red-stained cataclasite in listvenite, cut by white-yellowish dolomite veins; (e) listvenite cataclasite (marked red) reactivated by a sharp fault with quartz/carbonate vein (arrow); (f) black cataclasite in serpentinite; (h) red oxidized cataclasite in metasediments of the metamorphic sole.

171

172 Fluid inclusion thermobarometry of veins related to faulting in the Jebel Akhdar and Saih
173 Hatat domes indicates that much of the tectonic evolution occurred under the overburden of
174 the ophiolite (Grobe et al., 2019). Hence, the tectonic events observed in the carbonate
175 platform probably affected the ophiolite as well, although this has not been studied in detail.

176 **2.2. Listvenites in the Samail massif and Hole BT1B**

177 Listvenites are common in the northern part of the Samail massif of the Samail ophiolite,
178 Oman, where they form red- to orange-colored ridges that have a higher resistance to
179 weathering than peridotite. Historically, these listvenites were also called the Amqat unit
180 (Glennie et al., 1974; Stanger, 1985). The listvenites occur along the basal thrust of the
181 ophiolite where peridotite is in contact to the metamorphic sole (Nasir et al. 2007). The largest
182 outcrops are in lenses along the transition from the Jebel Akhdar to the Saih Hatat domes of
183 the Al Hajar mountain range (Falk & Kelemen 2015; Stanger 1985; Villey et al., 1986; Wilde
184 et al., 2002). Minor listvenite bodies also form tectonic blocks in shear zones within Hawasina
185 meta-sediments and the metamorphic sole of the same area (Nasir et al., 2007).

186 The listvenites at Wadi Mansah are an outstanding natural example showing that peridotite
187 carbonation reactions can go to completion on large scale (Falk and Kelemen, 2015). Where
188 listvenite is in contact with serpentinized peridotite, the presence of intergrown antigorite +
189 quartz ± talc suggests temperatures of 80 - 130 °C, broadly consistent with clumped-isotope
190 thermometry of carbonates (45 – 245 °C; Falk and Kelemen, 2015; Beinlich et al., 2020), and
191 the presence of microcrystalline quartz (recrystallized from opal or chalcedony) (Streit et al.,
192 2012). An internal Rb - Sr isochron gives an age of 97 ± 29 Ma (Falk and Kelemen, 2015), in
193 agreement with the age of emplacement of the ophiolite. Age corrected to 96 Ma, $^{87}Sr/^{86}Sr$
194 values in the listvenite are consistent with those of the underlying Hawasina metasediments
195 (Falk and Kelemen, 2015).

196 Hole BT1B of the Oman Drilling Project (International Continental Drilling Project
197 Expedition 5057-4B) was drilled in Wadi Mansah (lat. 23.3643°; lon. 58.1827°) in March
198 2017, to sample a continuous, un-weathered section of listvenite, serpentinite and the
199 metamorphic sole (Fig. 1a). The BT1B core has 100% recovery and includes about 200 m of
200 listvenite intercalated with serpentinite (Fig. 1b). An upper section of 70 m of listvenite is
201 followed by 20 m of carbonate-bearing serpentinite. A lower 80 m section of listvenite
202 includes several domains rich in chromian mica (light green layers in Fig. 1b), and is
203 underlain by 5 m of serpentinite. The lowermost 10 m of listvenite are separated from the
204 metamorphic sole by 10 cm of black cataclasite and clay fault gouge, which forms part of the

205   basal fault of the Samail ophiolite. Below the listvenites and fault gouge, the BT1B core
206   contains 100 m of the metamorphic sole, comprising 30 m of metasedimentary rocks and ~70
207   m fine-grained metamafic rocks (Fig. 1b). All of the listvenite-serpentinite contacts are intact
208   and gradational, and usually marked by domains of ophicarbonate.

209   While many calcite- and dolomite-bearing listvenites and birbirites (silicified serpentinite) in
210   the northern Samail massif have highly variable Mg/Si ratios and Ca contents (Falk &
211   Kelemen, 2015; Nasir et al., 2007; Stanger, 1985), the conversion of peridotite to magnesite-
212   rich listvenite at the site of Hole BT1B was nearly isochemical on the whole-core scale except
213   for the addition of CO_2. Average bulk rock Mg/Si, Fe/Si, Al/Si, Fe/Mg, and Cr/Al ratios in
214   listvenite are similar to the average composition of the Samail peridotite, while CaO and
215   correlated Sr are higher, most likely derived from underlying sediment (Falk & Kelemen,
216   2015; Godard et al., 2017; Kelemen et al. 2017, 2020). Thus Mg, Si, Al and Cr, plus Fe were
217   largely immobile on a ~ 10 m scale during introduction of C, O, lesser Ca, minor Fe, and
218   mobile trace elements during transformation of Mg-silicates to carbonate + quartz. This
219   implies a large solid volume expansion compared to unaltered peridotite.

3. Methods & Materials

3.1. Visual core logging

222   Cores of Hole BT1B were logged onboard R/V Chikyu in September 2017 by the Oman
223   drilling Phase 1 science team following IODP logging standards (Kelemen et al., 2020).
224   During the macroscopic core logging the host rock was characterized as massive, brecciated,
225   foliated, sheared, cataclastic, or fragmented by veins if the host rock structure was completely
226   obscured by a high vein density. For planar structures that crosscut the host rock, orientation
227   and width could be determined; of these, individual veins, sets of veins, cataclasites,
228   (semi)ductile shear zones, and sharp faults were distinguished. Cataclasites were identified
229   based on the observation of clast sliding and rotation, and fragmentation of particles into a
230   fine grained matrix (Passchier & Trouw, 2005). First results and datasets of the onboard core
231   logging are available in the online Initial Results volume of the Oman Drilling Project
232   (Kelemen et al., 2020). For this study, we revisited cataclastic structures identified in the
233   onboard logs by inspecting split core images in detail in order to improve the consistency of
234   the dataset with regards to these brittle structures.

3.2. Samples

236   Samples were selected during onboard drill core logging following different criteria, covering
237   the broad (micro)structural and textural diversity of the listvenites to identify the structures
238   related to different stages of carbonation reaction process as opposed to overprinting
239   structures after listvenitization. For this study, we inspected thin sections from 99 samples for
240   the presence of cataclasites. Thin sections from 27 samples that contain cataclasites have been
241   selected for detailed study (Supplementary Table S1).

3.3. Virtual polarizing microscopy (ViP)

243   A high-resolution virtual polarizing microscope platform (ViP) recently developed by the
244   Institute of Structural Geology, Tectonics and Geomechanics (GED, RWTH Aachen

245 University) and the Fraunhofer Institute for Life Science Informatics (Virgo et al., 2016) was
246 used for microstructural analysis.

247 The thin sections selected for this study were scanned in plane polarized and reflected light,
248 and with crossed polarizers at 10 different polarization angles, using a 10x objective. The
249 image data were then processed to extract the extinction curve of each "super pixel",
250 producing giga-pixel images of the extinction behaviour at all polarization angles, which
251 allows for multiscale image analysis. Virtual Petrography datasets and interpretations will be
252 shared publicly via the Oman Drilling Project data repository of the ICDP, together with a
253 virtual microscopy software (TileViewer) that is user friendly and allows Google Earth - like
254 zooming and browsing through the thin section as well as rotation of the polarisers and
255 switching between illumination conditions.

256 **3.4. Electron microscopy (SEM-EDS)**

257 A Zeiss Gemini SUPRA 55 field-emission electron microscope at the Institute of Structural
258 Geology, Tectonics and Geomechanics (RWTH Aachen University), was used for phase
259 identification and automated energy-dispersive X-ray spectroscopy (EDS) mapping of thin
260 sections. Samples were coated by a 6 – 8 nm thick layer of tungsten for conductivity.
261 Operating conditions were 3 kV and ~5 mm working distance for high magnification imaging,
262 and 15 kV and 8.5 mm working distance for EDS analysis, at high vacuum, respectively. A
263 dwell time of 200 μs/point was chosen for EDS mapping of whole thin sections.

264 **3.5. Image analysis and grain size distributions**

265 The EDS data and back-scattered images were processed by applying noise reduction filters
266 and defining thresholds in ImageJ to produce phase maps for the major minerals. Distinction
267 between quartz and amorphous silica, or between magnetite, hematite and Fe-hydroxides, was
268 not possible for large area EDS mapping. We used the particle analysis tool of ImageJ to
269 determine the grain size distribution in selected representative areas of cataclasite, following
270 an approach similar to that of Keulen et al. (2007). Due to the phase variability and the matrix
271 cementation by silica and Fe-(hydr)oxides in many cataclasites, particles were segmented
272 based on magnesite phase maps from EDS data, and on plain polarized ViP microscopy scans.
273 SEM-EDS data allows for higher resolution, whereas the giga-pixel ViP microscopy images
274 provide the particle size distribution of both mineral and lithic clasts on the whole thin-section
275 scale while filtering out the parts of the cataclasite affected by Fe-(hydr)oxide staining and
276 cementation. Late carbonate veins crosscutting the cataclasites have been filtered out based on
277 the particle aspect ratio. To measure the grain size distributions of clasts, the relative
278 frequency of grain areas normalized to the image area and the bin width have been calculated
279 as the number of grains N_i in each bin i, using 5 logarithmic spaced bins per order of
280 magnitude. Plotting the relative frequency against the grain area in log-log plots yields the
281 local linear slope D of a possible power law distribution (Keulen et al., 2008; Laurich et al.,
282 2018).

283

4. Results

4.1. Field relations

Listvenites in the Wadi Mansah and Fanjah regions of the Samail massif form meter to decameter thick bands within serpentinite and along contacts between serpentinite and the metamorphic sole (e.g., Fig. 1c). Commonly two or three such listvenite bands are intercalated in serpentinite and can be followed for several kilometres along strike. Contacts between listvenite and variably serpentinized peridotite are either gradational – composed of a 0.5 – 3 m wide transitional zone of carbonate-bearing serpentinite – or consist of strongly deformed, up to 3 m wide serpentinite fault gouge. Partially hydrated, layered peridotite (i.e. dunite-harzburgite with low degree of serpentinization) was not found in direct contact with listvenite; instead they are separated by a 3-20 m wide layer of (carbonate-bearing) serpentinite, locally with intergrown serpentine and quartz, and/or mineral assemblages including talc (Falk & Kelemen 2015; Manning et al., 2017). Contacts between listvenite and greenschist to amphibolite facies rocks of the metamorphic sole, Hawasina metasediments, layered gabbro, and Tertiary sediments are commonly characterized by faults with abundant cataclasites, and locally 0.3 m to > 5 m of serpentinite fault gouge. Broad folding of the basal fault of the ophiolite north of Wadi Mansah may have locally inverted the original shear sense of these faults. At the southern fold limb, drag folds and striae on slip surfaces at the contacts to the metamorphic sole indicate an apparent top-down sense of shear (Fig. 1c).

Faults and cataclasites (< 5 mm to > 2 m wide) are common in the listvenites in the Samail massif (e.g. Fig. 1d & e). Striae on fault planes in listvenite suggest an apparent normal, oblique normal or strike-slip sense of shear. Locally, nearly vertical strike-slip faults cut the faults that form the contact between listvenite and the metamorphic sole, with offsets of several meters, indicating that faulting along the contact occurred during an earlier phase of deformation. In general, tilting and rotation of large fault blocks, folding, and the lack of clearly defined marker horizons make it difficult to reconstruct the true sense of shear for the faults in listvenites and serpentinites. Cataclasites in listvenites are cohesive and their sense of shear is often not possible to determine in outcrops. Lithic listvenite clasts in cataclasite are slightly rounded to angular and up to 5 – 10 cm in diameter. The cataclasites are cemented by a matrix that is often stained red (silica-rich cataclasites with Fe-oxides) or yellow (dolomite-rich cataclasites) in outcrops. In the field, cataclasites are also widespread along fault zones within schist of the metamorphic sole, where they crosscut the metamorphic foliation (Fig. 1g), and in late Paleocene conglomerates that unconformably overlie the ophiolite NE of the village of Fanjah. In serpentinite, it is difficult to detect clear and cohesive cataclasites due to weathering, but occasionally, black (ultra)cataclasites are discernible (Fig. 1f).

4.2. Hole BT1B

Core logging has revealed a diverse petrology and structure, from serpentinite with peridotite relics, massive listvenite, foliated listvenite, several generations of veins, ductile shear zones, cataclasite, breccia and planar faults (Kelemen et al., 2020).

The density of veins in the core is very high, > 100 per m (Manning et al., 2017). Both the serpentinite and listvenite in the core contain and are overprinted by several generations of veins, cataclasites, sharp planar faults and late, partially open veins. The earliest type of magnesite vein, which occurs in both serpentinite and listvenite, is antitaxial. In the upper part

327 of Hole BT1B, this earliest vein type includes a median line rich in iron oxides (haematite,
328 goethite). Quartz + chalcedony +/- carbonate veins are syntaxial and younger, based on cross-
329 cutting relationships. These structures are overprinted by cataclasites and breccia, often
330 enriched in iron oxides, and sharp, planar faults with silica or carbonate veins on the slip
331 surface. Syntaxial, partially open veins of magnesite or dolomite are the latest structures.
332 Cross-cutting relations may not be the same everywhere in the core, and structures belonging
333 to one generation may or may not be synchronous.

334 Listvenite not affected by overprinting (i.e. "primary listvenite") can be massive, containing
335 spheroidal magnesite grains and pseudomorphs of the typical mesh and bastite textures of
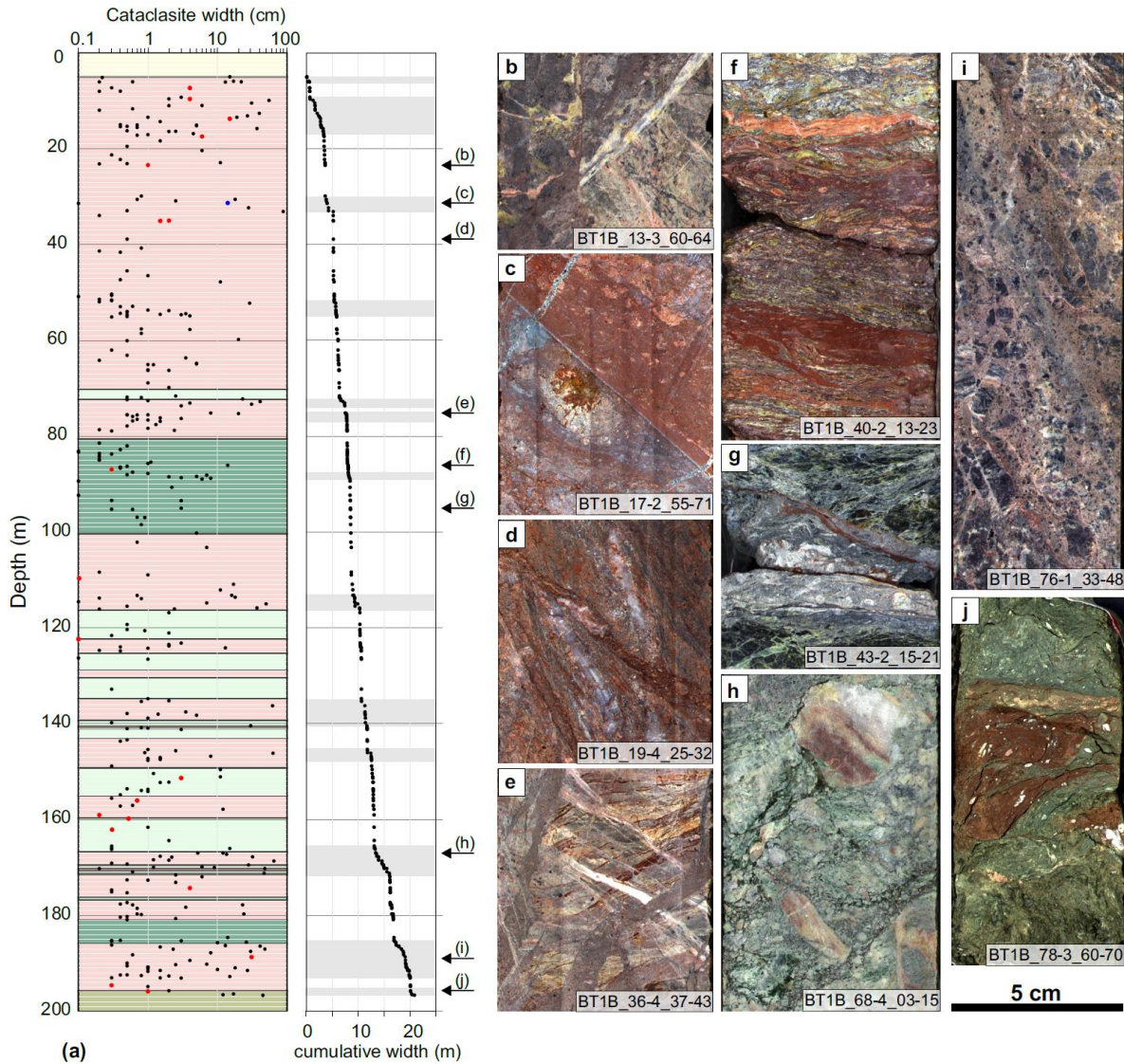
Fig. 2 Macroscopically identified cataclasites in the upper 200 m of Hole BT1B. (a) Plots of occurrences and width of all logged cataclasites (red data points show cataclasites confirmed in thin section; color coding of lithologies as in Fig. 1b) and their cumulative width with depth in Hole BT1B (grey shadings highlight intense brittle deformed intervals); (b - e) core scan images of examples of cataclasites in the upper listvenites; (f & g) cataclasite in the upper serpentinite layer; (h & i) cataclasite in the lower listvenites; and (j) fault gouge at the contact to the metamorphic sole.

336 serpentinite (Beinlich et al., 2020; Jöns and Bach, 2013; Lafay et al., 2020). In other parts of
337 the core, primary listvenite has a well-developed foliation defined by lithological banding and
338 at the microscale ellipsoidal carbonate particles with an iron oxide core. Shear bands with a
339 locally well-developed foliation are common in the serpentinite, and also in the transition
340 between serpentinite and listvenite, where there are no discernible faults or cataclasites.

4.2.1. Macroscopically identified cataclasites in Hole BT1B

342 Figure 2 shows a plot of the occurrences of macroscopically identified cataclasites with depth
343 and split-core images of cataclasites in listvenite and serpentinite in Hole BT1B. Cataclasites
344 occur throughout most of the core, with particularly thick or abundant cataclasite intervals
345 between 5 – 18 m, 51 – 55 m, 146 – 151 m, 166 – 172 m, and 185 – 192 m depth (Fig. 2a). A
346 55 cm wide fault gouge (Fig. 2j) forms the contact between listvenite and the metamorphic
347 sole at 197 m depth. This clay-rich, granular gouge is texturally distinct from the cohesive
348 cataclasites within listvenite core.

349 In total 352 cataclasites were identified macroscopically in the upper 200 m of Hole BT1B,
350 with a cumulative width of about 21 m (Fig. 2a). Hence, about 10 vol% of listvenite and
351 serpentinite in Hole BT1B is composed of cataclasite. This estimate only includes sections
352 where clast rotation and a high degree of fragmentation typical of cataclasis occurred; the
353 additional thickness of damage zones with cracked grains and a high abundance of small-scale
354 faults in the rock adjacent to cataclasites is often substantial.

355 The width of single cataclasite bands varies significantly throughout the core (0.1 cm – 1 m).
356 For wide cataclasites, orientation and true thickness could not be determined from the core
357 sections and the estimated true width is somewhat uncertain. The lack of macroscopically
358 visible cataclasites does not exclude their presence: in several cases, < 1 mm wide cataclasite
359 bands are visible in thin sections of samples without macroscopically visible cataclasis. Most
360 cataclasites are cohesive and form anastomosing and branched bands (Fig. 2d, e). Wide
361 cataclasites (> 3 cm) occasionally display internal flow banding of small grained matrix-rich
362 domains that envelop coarse, variably cracked clasts (Fig. 2 c, i). Locally several cataclasite
363 generations overprint each other and are crosscut by sharp faults (e.g. Fig. 2c). Fe-hydroxide
364 staining is common in the matrix of many cataclasites, in particular in the upper 60 m of Hole
365 BT1B. The amount of displacement related to cataclasites is rarely measurable in the core
366 (e.g. Fig. 2d), perhaps because many have displacements larger than the 6.4 cm (HQ) and 4.8
367 cm (NQ) core diameter. However, there are no cataclasites containing listvenite or
368 metamorphic sole lithologies within serpentinite host rocks, none containing serpentinite or
369 sole lithologies within listvenite, and none containing listvenite or serpentinite within the sole,
370 suggesting that displacements along the cataclasites near contacts are less than a few meters.

4.2.2. Microstructure of cataclasites in listvenites

372 Cataclasites are composed of quartz/chalcedony, magnesite, dolomite and oxide mineral clasts
373 (grain sizes ranging from below 0.2 to 500 μm), and different lithic clasts of variable size.
374 Magnesite mineral clasts are very common in cataclasite, whereas larger quartz clasts are rare
375 (probably due to the generally small grain size of quartz/chalcedony in the host listvenite).
376 Lithic clasts can contain fragments of listvenite composed of magnesite spheroids and
377 interstitial quartz – a common microstructure in listvenite of Hole BT1B (Fig. 3). Larger
378 clasts occasionally contain fragments of veins that crosscut the listvenite. Other lithic clasts

379 are fragments of magnesite veins, chalcedony-magnesite veins, quartz veins, breccia and
380 cataclasite. Clasts are commonly rotated and rounded – in particular where cataclasites have
381 been reactivated several times (Fig. 3c). Magnesite mineral clasts locally show a chemical
382 zonation of Fe contents — similar to magnesite in host listvenite (e.g. Beinlich et al., 2020;
383 Lafay et al., 2020). The Fe zonation is truncated sharply at the rims of magnesite clasts (Fig.
384 4b). Relict Cr-spinel is strongly fragmented (grain sizes < 5 to > 500 µm) and can serve as a
385 strain indicator where stretched into trails of dismembered grains (Fig. 4a). Red staining of
386 some cataclasites is due to fine grained hematite and goethite (< 20 µm) that decorate clast
387 rims and occur interstitially in the fine-grained matrix. In contrast to angular and fragmented
388 Cr-spinel, hematite in the cataclasite matrix displays subhedral to euhedral grains that are
389 partly rounded or form small acicular and atoll shaped aggregates (Fig. 4b). The smallest
390 grain size fraction (matrix) is commonly dominated by quartz/chalcedony and a smaller
391 proportion of magnesite fragments. Dark-coloured, discontinuous ultracataclasite seams and
392 bands (< 100 µm wide) occur within cataclasites and at their boundary with the listvenite host
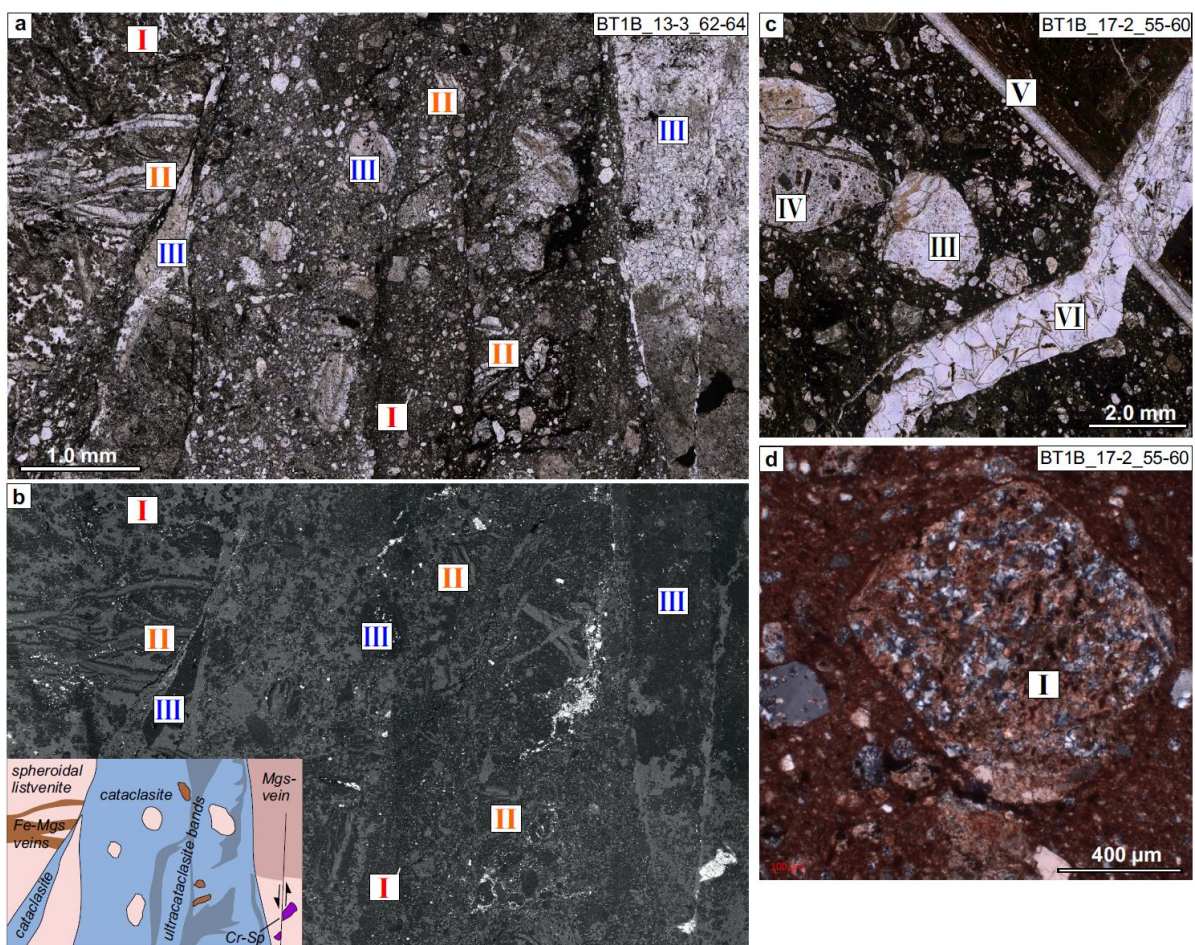
Fig. 3 Listvenite cataclasite microstructures. (a & b) ViP plane polarized (ppol) micrograph and BSE image of localized cataclasite, showing clasts of listvenite with magnesite spheroids (I) and vein fragments (II, III), and corresponding microstructures in the host listvenite. A simplified interpretative sketch is given in the inset in b). (c) Reworked cataclasite with breccia clast (IV). A sharp fault with dolomite-calcite and quartz veins (V), and a dolomite vein (VI) crosscut cataclasite (ViP ppol). (d) Clast with magnesite spheroids and Fe-hydroxide staining in cataclasite matrix (crossed polarizers).
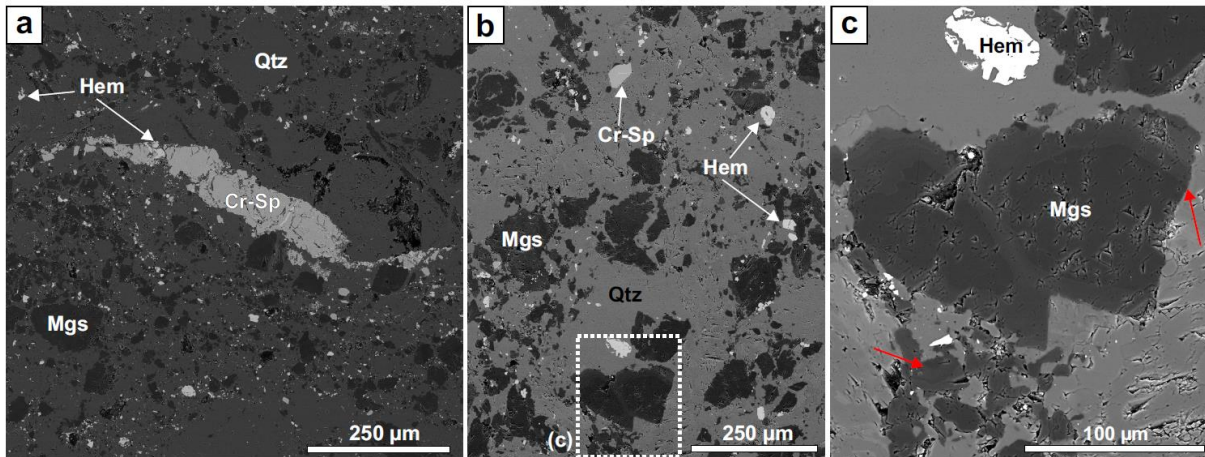
Fig. 4 BSE images of Fe-(hydr)oxide stained cataclasites. (a) Stretched and fragmented Cr-spinel suggesting sinistral shear (sample BT1B_17-2_55-60). (b) Angular fragments of Cr-spinel vs. rounded to subhedral hematite grains and aggregates in cataclasite matrix. (c) Detail from b), showing truncation and fragmentation of chemically zoned magnesite clast (red arrows). (b & c: sample BT1B_9-3_28-31; in these images contrast and brightness have been adjusted to enhance visibility of the zonation in magnesite).

393   rock, commonly oriented sub-parallel to the main cataclasite. Sharp faults often crosscut
394   cataclasites or are localized along their contact with the host listvenite.

395   Clast sizes from 50 – 50000 μm² in a prominent cataclasite at 31.4 m depth (sample
396   BT1B_17-2_55-60) follow a power law distribution with D values of ~1.9 – 2.0 (Fig. 5). Such
397   D values are typical for cataclasites and fault gouges that are characterized by extensive clast
398   rotation and displacement (e.g. Billi, 2007; Keulen et al., 2008; Laurich et al., 2018).
399   Cataclasites that overprint pre-existing cataclasite contain fewer large clasts and a higher
400   matrix fraction.

401   ### 4.2.3. Cross-cutting relationships

402   With the exception of the youngest generation of carbonate veins (usually dolomite or
403   dolomite-calcite), most other microstructures in host listvenite are truncated by cataclasites,
404   and fragmented clasts of these earlier structures are present within the cataclasites. The
405   microstructures overprinted by cataclasite include host listvenite with a spheroidal to euhedral
406   magnesite habit (Fig. 3a-I, Fig. 3d), antitaxial magnesite veins displaying Fe zonation (Fig.
407   3a-II), microcrystalline quartz veins, and magnesite-chalcedony veins (Fig. 3a-III). Besides
408   truncation and fragmentation of host listvenite structures, different cataclasite generations
409   overprint each other, with thin localized cataclasite bands crosscutting or reactivating older
410   ones (cf. breccia clast in cataclasite, Fig. 3c-IV).

411   Figure 6 is a good example of the youngest microstructures and their cross-cutting relations in
412   Hole BT1B, showing a sharp fault juxtaposing two distinct cataclasite generations (α & β in
413   Fig. 6). The highly localized slip plane is marked by an up to 1.5 mm wide, red-stained
414   ultracataclasite band (γ, Fig. 6), and by a 250 μm wide vein of microcrystalline quartz
415   precipitated after faulting. Cataclasites, fault and the quartz vein were then crosscut by
416   syntaxial, coarse-grained dolomite veins. The youngest microstructure is a dolomite-calcite
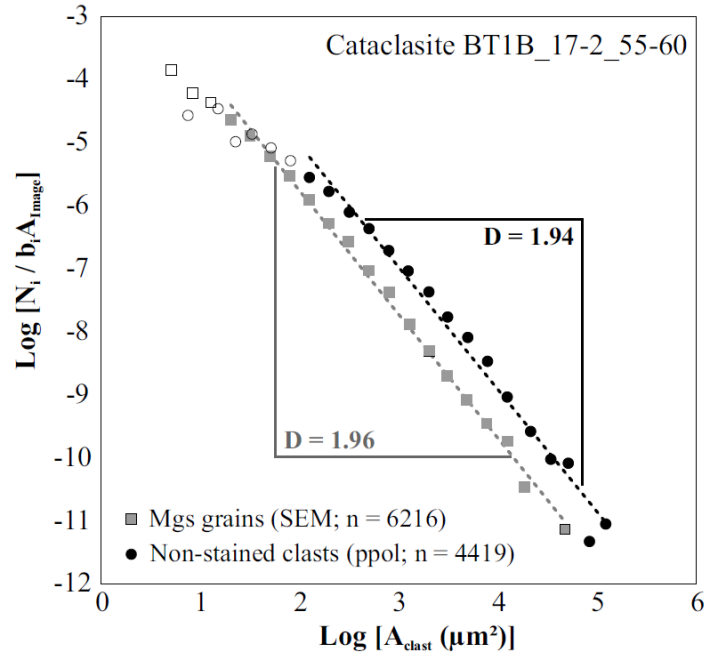
Fig. 5 Grain size distribution of listvenite cataclasite, showing a log-log plot of clast frequency N_i versus area A. Frequency is normalized to the bin width and the image area, for 5 logarithmic bins per order of magnitude. Similar D values (slope of the power-law fit to curves) are obtained from image segmentation of magnesite grains (by SEM-EDS mapping), and from clasts that are not stained by Fe-hydroxides (by plain polarized mosaic microscopy image, ViP) when the smallest, least reliable grain fractions are excluded.

417   vein that partly follows the quartz vein along the fault plane and deflects into the dolomite
418   vein. This is consistent with the observation that the youngest veins in field outcrops and
419   throughout Hole BT1B often are composed of dolomite (±calcite), forming syntaxial veins,
420   partially open veins and the matrix of hydraulic/hydrothermal breccias.

421   **4.2.4. Chemical characteristics of cataclasite**

422   SEM-EDS chemical mapping shows that in many cases, fluid flow during or after cataclasis
423   modified the Mg/Si ratio of listvenite affected by brittle deformation. Different cataclasite
424   generations that overprint each other are affected to variable extent by this chemical
425   modification. Reconstructed EDS spectra of two ~400 mm² areas of different cataclasite
426   generations juxtaposed by a fault in a large thin section of sample BT1B_17-2_55-60 reveal
427   that grey-red cataclasite with a more abundant coarse clast fraction has a molar Mg/Si ratio of
428   ~ 0.49 (α in Fig. 6). This is significantly lower than the average molar Mg/Si of harzburgite
429   (1.52 – 1.54) and dunite (1.75 – 1.80) of the Samail ophiolite (Godard et al., 2000; Hanghøj et
430   al., 2010; Monnier et al., 2006), and lower than average listvenite in Hole BT1B (~ 1.48;
431   Kelemen et al., 2020). Red-stained, finer grained cataclasite in the area above the fault shows
432   more rounded mineral and lithic clasts, and has even lower Mg/Si of ~ 0.18 (β in Fig. 6). And
433   the Mg/Si ratio is as low as 0.01 in the 1.5 mm wide, silica-dominated ultracataclasite band
434   adjacent to the fault slip plane, which is mostly composed of a fine-grained matrix with only
435   few clasts (γ, Fig. 6). A similar, variable enrichment of Si relative to Mg in comparison to the
436   host listvenite is evident in most of the cataclasites we studied in detail (e.g. Fig. 7a & b). In
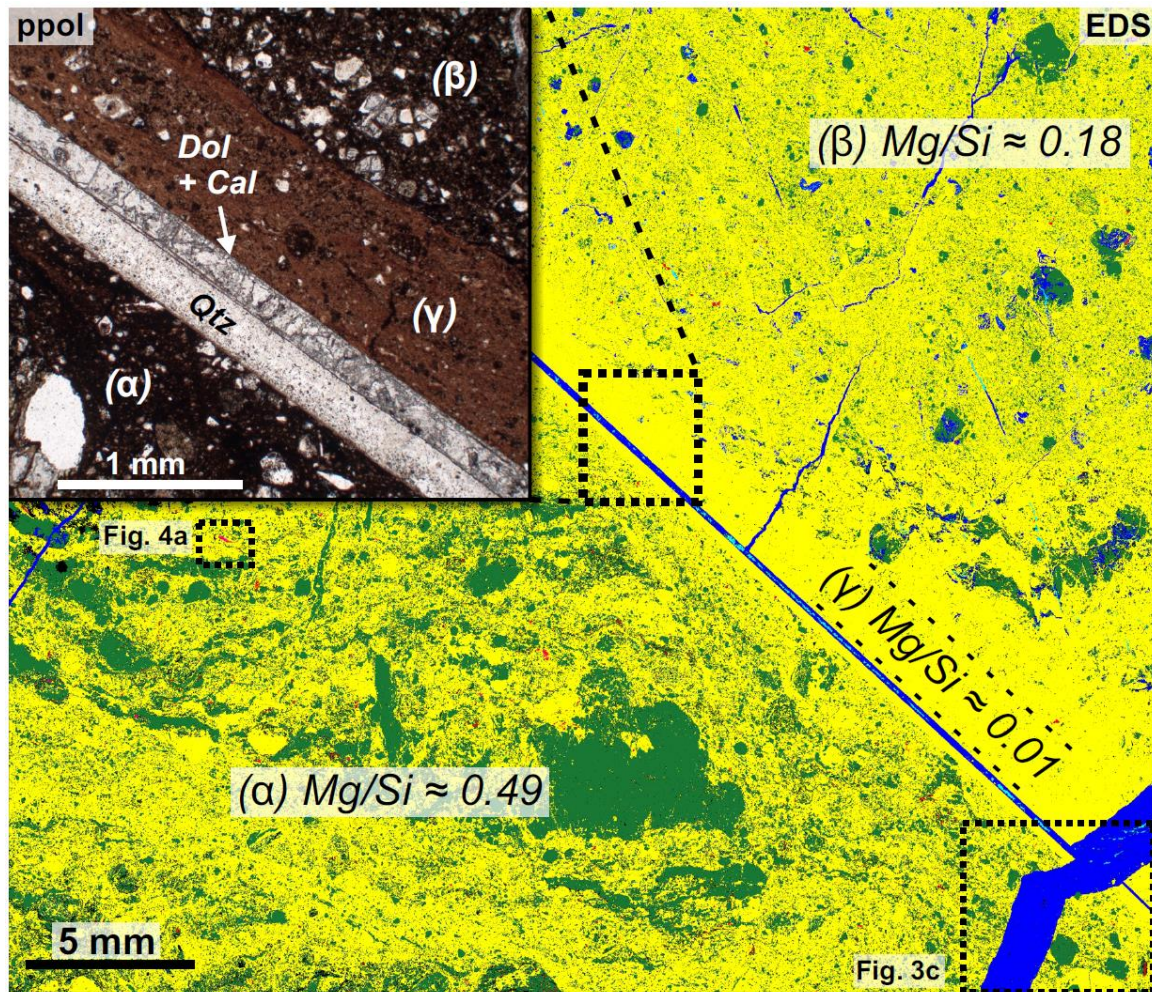
Fig. 6 Variation of silica and carbonate contents in reworked cataclastic listvenite. Large area EDS phase map of two cataclasite generations (α, β) separated by an ultracataclasite (γ) and a fault (sample BT1B_17-2_55-60), showing quartz (yellow), magnesite (green), dolomite (dark blue), calcite (cyan), Fe-oxide (red) and Cr-spinel (magenta). The inset in the upper left shows a detail ppol image of the ultracataclasite (γ), and quartz and calcite-dolomite veins along the sharp fault. Average Mg/Si values were calculated using reconstructed EDS spectra integrated over representative areas of the different reworked cataclasite generations.

437   addition, locally thin (< 2 mm) ultracataclastic bands composed of quartz clasts cemented by
438   a Cr-Al-Fe-hydroxide nanoscale phase cut previous cataclasite generations (Fig. 7). The nano-
439   phase is slightly enriched in Zn, and occurs in cataclasite that may contain kaolinite, but
440   where chromian mica is absent. Small clasts of Cr-spinel are similarly abundant in these
441   bands as in other cataclasites. In sample BT1B_17-2_55-60 thin veins of a similar Cr-Al-Fe-
442   hydroxide locally crosscut cataclasite, but are truncated by the sharp fault.

443   Dolomite-cemented breccias occur throughout listvenite in core from Hole BT1B. In
444   macroscopic observation, these can be similar to listvenite cataclasites, with partially rotated,
445   angular fragments of highly variable grain size. However, EDS chemical mapping revealed
446   that their matrix is consistently composed of dolomite – in contrast to fine grained quartz and
447   magnesite clasts in cataclasite – and the breccias display a continuous variation in texture,
448   grading into the late dolomite vein network (Fig. 8). We interpret these breccias to have

449 formed by overpressured hydrothermal fluid with little tectonic displacement, as opposed to
450 the earlier listvenite cataclasites, which require high strain.

451
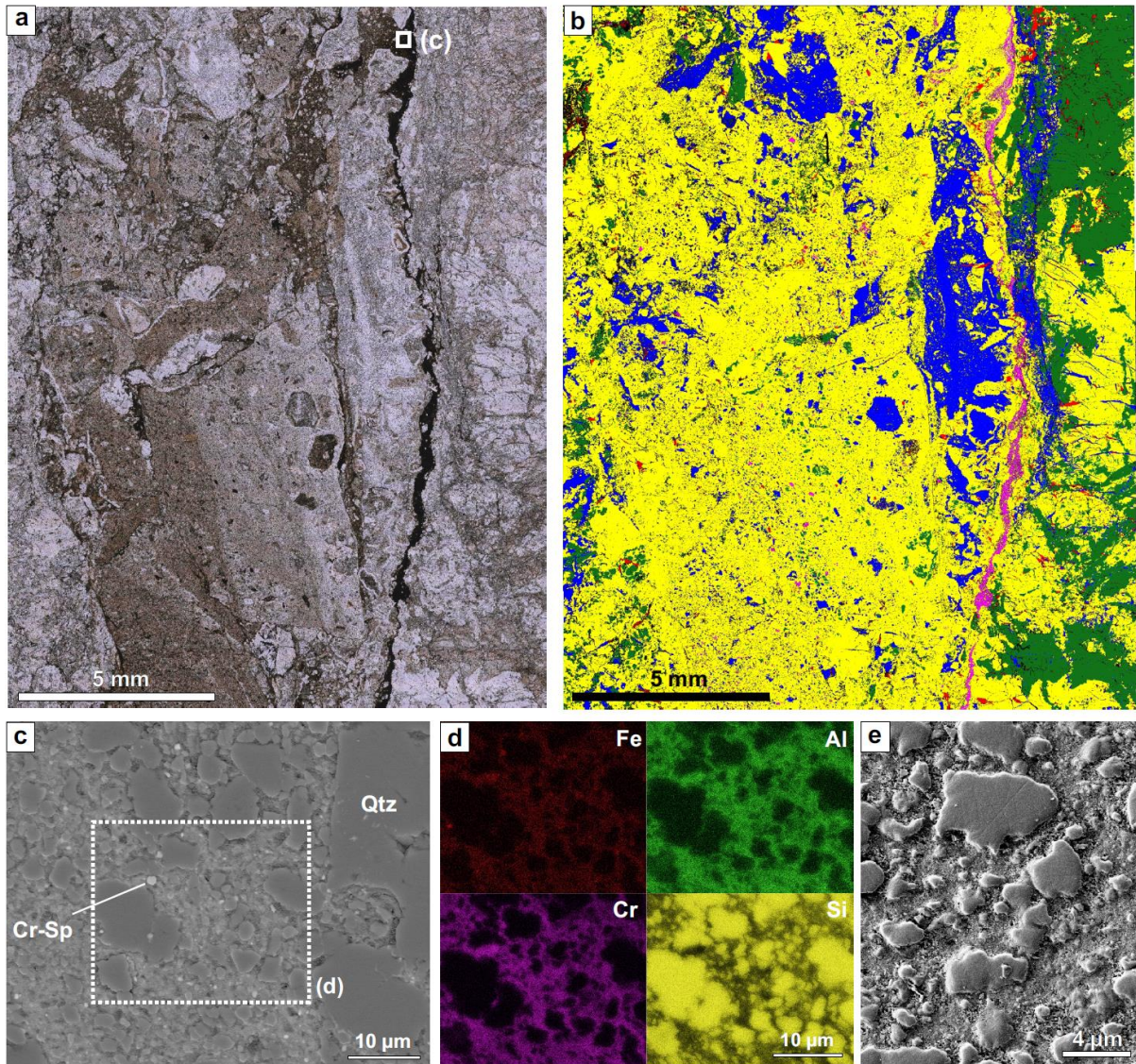
Fig. 7 Vertically oriented and multiply reactivated listvenite cataclasite with late, dark ultracataclastic band (sample BT1B_65-2_22-26). (a) Plain polarized overview (ViP). b) Phase map from SEM-EDS mapping (yellow = quartz; green = magnesite; blue = dolomite; red = kaolinite/clay; magenta = Cr-rich phases). The cataclasite is reworked and has significantly less magnesite than the host listvenite on the right and left sides of the image. (c) BSE image of dark ultracataclastic band in a); darker clasts are quartz/silica. (d) EDS chemical maps of area in c) showing cementation of quartz clasts by an interstitial Cr-Al-Fe nano-phase. (e) SE image of quartz µ-clasts cemented by the interstitial Cr-Al-Fe-phase.

5. Discussion

5.1. Relative timing of listvenite formation and cataclasis

Cataclastic deformation could in principle provide a positive feedback for the replacement of peridotite by listvenite due to mechanically enhanced reaction rates, if cataclasis was coeval with carbonation (Lisabeth et al., 2017). However, in the case of the thin sections we analysed, composed of macroscopically well-defined cataclasites of Hole BT1B, the microstructures consistently show that cataclasis occurred in previously formed listvenites. This is shown by truncated clasts of listvenite with spheroidal magnesite, fragments of magnesite and chalcedony–magnesite veins that elsewhere crosscut listvenite, and reworked breccia fragments, all within cataclasites. The observation of truncated growth zonation at the rims of fragmented magnesite clasts (Fig. 4b) provides further evidence that cataclasites formed after listvenite formation.

The widespread occurrence of cataclasites throughout listvenites of the core from Hole BT1B, and the common reactivation and reworking of older cataclasites by younger cataclasites and faults, indicates a multiphase, distributed, brittle, post-listvenite deformation in Hole BT1B, perhaps in a relay zone between larger faults. Our study shows that the most evident records of brittle shear—cataclasites composed of listvenite fragments—formed after the formation of listvenite. Nevertheless, it is possible that earlier examples of cataclasites occur elsewhere in the Oman listvenite, and that cataclasis before or during listvenite formation may have been obscured in the core due to subsequent overprint by veins or dissolution-reprecipitation reactions.

5.2. Fluid flow and chemical modification in listvenite cataclasites

SEM-EDS chemical mapping revealed that in most of the studied samples, cataclasites have a significantly lower Mg/Si ratio than the host listvenite, indicating the local dissolution of magnesite and/or addition of SiO_2. The results show that repeated reactivation and reworking to subsequently finer grained cataclasite was correlated with increased Mg loss and/or silica enrichment (Fig. 6), suggesting that this bulk chemical modification was related to the fluids present during and shortly after cataclastic deformation. Thermodynamic reaction path modelling at relatively low temperatures (100 °C) suggests that extremely high fluid/rock ratios could lead to complete carbonate dissolution together with silica enrichment (i.e. birbirite formation) produced by the same fluids that form listvenite at lower fluid/rock ratios (Klein & Garrido, 2011). Because the solubility of silica increases with temperature while that of magnesite decreases, and the thermodynamic models of Klein & Garrido (2011) predict birbirite formation and low pH at 100°C, but not 200, 300 or 400°C, the observed silica addition and/or Mg loss in cataclastic listvenite are consistent with the geothermometry constraints to 80 – 130 °C for listvenite formation (Falk & Kelemen, 2015).

Thin, ultracataclastic bands cemented by a Cr-Al-Fe-hydroxide nano-phase that represent the last cataclasite generation (Fig. 7) likely formed from low pH fluids. At 90 °C, experiments and thermodynamic calculations indicate that Cr is ~4 orders of magnitude more soluble in aqueous fluids at pH 4 than at pH 6, whereas it is largely insoluble at neutral and moderately alkaline pH (Rai et al., 1987). Therefore, Cr mobilization in aqueous fluids is incompatible with the slightly alkaline conditions buffered by carbonate dissolution and likely minor in high pH fluids produced by serpentinization (Chavagnac et al., 2013; Giampouras et al., 2020;

495 Paukert et al., 2012). The absence of chromian mica and the presence of kaolinite in the
496 vicinity of ultracataclasite bands cemented by the Cr-Al-Fe-hydroxide nano-phase (Fig. 7b) is
497 consistent with the higher dissolution rates of mica at lower pH (Pachana et al., 2012),
498 suggesting Cr remobilization due to mica dissolution in addition to chromite alteration. A
499 slightly acidic pH of fluids related to cataclasite cementation is further in agreement with the
500 inferred local carbonate dissolution (Fig. 6), and indicates that fluids were out of equilibrium
501 with listvenite during this stage of reaction and deformation. We interpret the observation that
502 Cr-Al-Fe-hydroxide veins are rare, while Cr-spinel fragments are common in cataclasites, to
503 be due to the pH buffer capacity of magnesite dissolution, which prevented larger scale re-
504 mobilization of Cr.

505 The observation that dolomite and dolomite-calcite veins often crosscut cataclasites (Fig. 8),
506 breccias, and faults, suggests that part of the Ca gain with respect to mantle peridotite, as
507 observed in the Oman listvenites (Falk & Kelemen, 2015; Godard et al., 2017; Kelemen et al.,
508 2017; Kelemen et al., 2020), may be related to late fluids after the main listvenite formation
509 occurred. Some of the young dolomite and dolomite-calcite may have precipitated from fluid
510 derived from unconformably overlying Tertiary limestone (de Obeso and Kelemen, 2018) or
511 may be of meteoric origin, similar to the widespread surface-near occurrence of carbonate
512 veins and travertine deposits in the Oman peridotites (Giampouras et al., 2020; Noël et al.,
513 2018; Streit et al., 2012). Scharf et al. (2020) report a U/Pb age of 55±4 Ma for calcite veins
514 cutting listvenite near the village of Fanjah, consistent with the hypothesis that fluid flow
515 during Eocene deformation may have redistributed Ca in the listvenites, and/or introduced
516 additional Ca from sediments above or below the ophiolite.
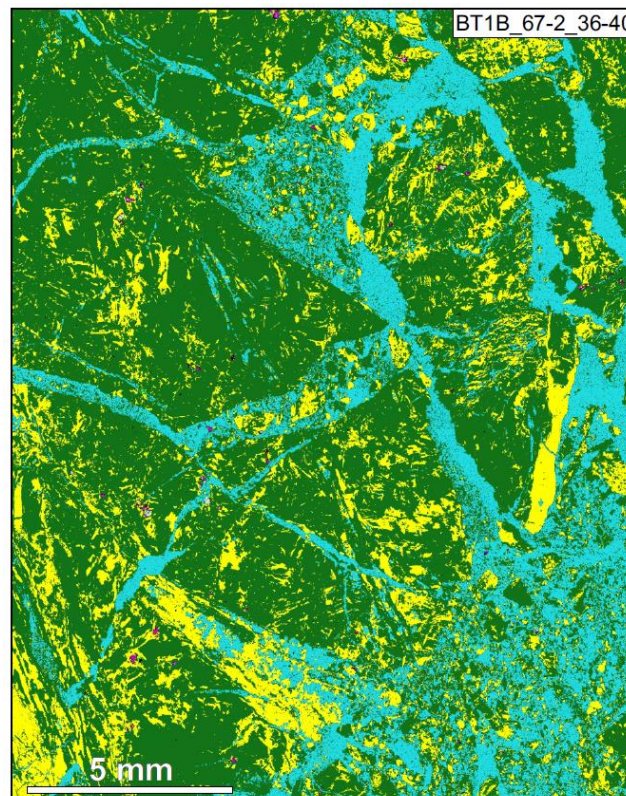
Fig. 8 SEM-EDS phase-map of dolomite-cemented breccia in listvenite, with quartz (yellow), magnesite (green), dolomite (light-blue) and Cr-spinel (magenta).

5.3. Relationship with post-obduction tectonics

517
518 In the absence of absolute dating of the cataclastic listvenite, three main, protracted tectonic
519 phases could be related to cataclastic deformation of the basal peridotites and listvenites: (i)
520 brittle thrusting during ophiolite obduction (Fig. 9a), (ii) post-obduction extensional shear
521 zones or reactivation ("retrocharriage") of previous reverse faults (e.g., Gray & Gregory,
522 2003) (Fig. 9b), and/or (iii) late oblique normal or strike slip faulting related to uplift of the
523 Jebel Akhdar and Saih Hatat anticlinoria (Fig. 9c, d).

524 Ophiolite obduction onto the continental platform was followed by ductile top to the NE-
525 shear along listric shear zones, normal to oblique-slip faults of late Cretaceous to early
526 Paleogene age, and subsequent strike-slip faults during the Eocene in limestone (Fig. 9b – d;
527 cf. Sec. 2.1), accompanying the exhumation of the autochthonous continental margin in the
528 Jebel Akhdar and Saih Hatat anticlinoria (Gomez-Rivas et al., 2014; Grobe et al., 2018; Grobe
529 et al., 2019; Hansman et al., 2018). Because the strength of magnesite is significantly higher
530 than that of calcite limestones (Holyoke et al., 2014), extensional deformation recorded by
531 ductile top to the NE- shear zones in the carbonate platform (Fig. 9b) may have been related
532 to cataclasis in listvenite, possibly reactivating earlier structures.

533 Cataclasites could have continued to form during subsequent faulting of the carbonate
534 platform in the early Paleogene to Eocene (Fig. 9c), which may be recorded by some of the
535 faults in listvenite and at many of the contacts between listvenite, serpentinite and the
536 metamorphic sole (Fig. 1a & c). The abundance of calcite veins in the Cretaceous section
537 below the ophiolite (Grobe et al., 2018) points to a significant amount of fluid flow during
538 this phase. Fluid inclusion thermometry in quartz and calcite veins in the limestones indicate
539 cooling from about 220 – 130 °C during the transition from normal to strike-slip faulting
540 during exhumation of the Jebel Akhdar (Grobe et al., 2019). In the Saih Hatat, uplift and
541 cooling started somewhat earlier, reaching 120 – 90 °C in the Eocene (Hansman et al., 2017).
542 Reactivation of listvenite cataclasites by sharp faults and the formation of dolomite-cemented
543 breccias in the Wadi Mansah area may be partly related to the uplift of the erosional surface
544 atop the Jebel Akhdar and Saih Hatat anticlinoria to their current high topography (Fig. 9d)
545 and the development of the Samail gap fault zone (Scharf et al., 2019).

5.4. Cataclasis – a positive feedback mechanism for carbonation?

546
547 The close spatial relation of listvenites with the basal thrust and other faults in Oman and
548 other ophiolites (Ash & Arksey, 1989; Menzel et al., 2018; Qiu and Zhu, 2018) suggests that
549 the interplay between major tectonic deformation and fluid flux may play a key role in large
550 scale formation of listvenites. In these settings, cataclasites and dilatant faults and veins are
551 likely to occur, which may enhance reactivity with CO_2-bearing fluids (Lisabeth et al., 2017).
552 On the other hand, our results demonstrate that a tectonic overprint post-dating listvenite
553 formation —and related fluid flow and chemical modification—can be substantial and should
554 be filtered out in order to understand the mechanisms that sustain fluid flow and carbonation
555 reactions. In contrast, earlier veins, such as antitaxial magnesite veins, formed along fractures,
556 and record brittle deformation that may have played an important role in maintaining or
557 enhancing permeability and continued influx of CO_2-bearing fluids required for listvenite
558 formation.

559
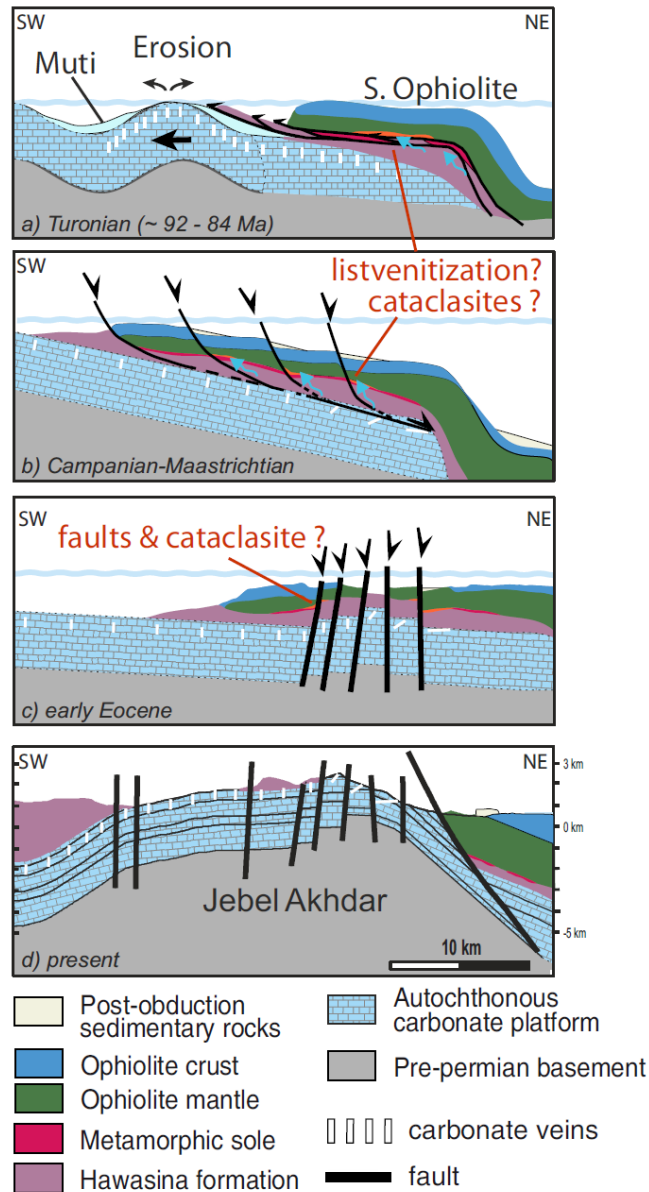
Fig. 9 Sketch of the simplified post-obduction tectonic evolution of the Samail ophiolite and carbonate platform in Oman (after Grobe et al., 2018), with potential stages of brittle deformation in listvenite at the base of the ophiolite (orange).

560

6. Conclusions

561

562 1. Visual core logging shows that about 10 vol% of listvenite and serpentinite throughout
563   Hole BT1B has been converted to cataclasite. Continuous core sections >1 m without
564   cataclasites are rare. The width of cataclastic bands in listvenite ranges from < 1 mm to >
565   100 cm. Brittle grain size reduction led to a power-law grain size distribution in
566   cataclasites with rounded clasts. We interpret this to be formed by multiple phases of
567   movement in an array of small (dm – m scale) faults.

568   2. In all samples with thin sections of macroscopically identified cataclasites, the
569   microstructures show that cataclasis overprints previously formed listvenites, as indicated
570   by truncated clasts of host listvenite with spheroidal magnesite habit, fragments of
571   chalcedony–magnesite veins, and reworked breccia fragments in cataclasite.

572   3. Sharp faults, dolomite veins and dolomite-calcite veins crosscut listvenite cataclasites and
573   are the youngest brittle deformation structures in the core.

574   4. SEM-EDS chemical mapping reveals that cataclasites commonly have a lower Mg/Si ratio
575   than the host listvenite, indicating the local dissolution of magnesite and/or addition of
576   SiO_2 in cataclasites by reactive fluids.

577   5. Thin ultracataclastic bands with an interstitial Cr-Al-Fe hydroxide nano-phase are the last
578   cataclasite generation. The mobilioty of Cr and Al in this process suggests that they
579   formed from acidic aqueous fluids (pH $\leq$ 4) related to dissolution of magnesite and
580   chromian mica.

581   6. Repeated brittle overprinting and reactivation of cataclastic listvenite in the field and Hole
582   BT1B core show that there were multiple brittle deformation events post-dating listvenite
583   formation in the basal section of the Samial ophiolite. Some or all of this multistage brittle
584   overprint of listvenite by cataclasites, faults and late veins may be related to the evolution
585   of the sedimentary continental margin units underlying the ophiolite after obduction.

586   7. Post-obduction brittle deformation with related fluid flow and local chemical overprint is
587   likely common in the basal section of the Samail ophiolite, Oman, and should be excluded
588   when analyzing earlier structures to understand the chemo-mechanical process of
589   listvenite formation.

590

Acknowledgments

Supplementary material

Supplementary Table S1: Overview of studied thin sections of samples with cataclastic structures **[will be uploaded to a PANGEA repository]**

References

Agard, P., Searle, M. P., Alsop, G. I., & Dubacq, B. (2010). Crustal stacking and expulsion tectonics during continental subduction: P-T deformation constraints from Oman. *Tectonics, 29*(5). doi:10.1029/2010TC002669

Akbulut, M., Piskin, O., & Karayigit, A. I. (2006). The genesis of the carbonatized and silicified ultramafics known as listvenites: a case study from the Mihaliccik region (Eskisehir), NW Turkey. *Geological Journal, 41*(5), 557-580. doi:10.1002/gj.1058

Al-Wardi, M., & Butler, R. W. H. (2007). Constrictional extensional tectonics in the northern Oman mountains, its role in culmination development and the exhumation of the subducted Arabian continental margin. *Geological Society, London, Special Publications, 272*(1), 187. doi:10.1144/GSL.SP.2007.272.01.11

Alt, J. C., Schwarzenbach, E. M., Früh-Green, G. L., Shanks Iii, W. C., Bernasconi, S. M., Garrido, C. J., . . . Marchesi, C. (2013). The role of serpentinites in cycling of carbon and sulfur: Seafloor serpentinization and subduction metamorphism. *Lithos, 178*(0), 40-54. doi:10.1016/j.lithos.2012.12.006

Andreani, M., Luquot, L., Gouze, P., Godard, M., Hoisé, E., & Gibert, B. (2009). Experimental study of carbon sequestration reactions controlled by the percolation of

629   CO_2-rich brine through peridotites. *Environmental Science & Technology, 43*(4),
630   1226-1231. doi:10.1021/es8018429

631 Ash, C. H., & Arksey, R. L. (1989). The Atlin ultramafic allochthon: ophiolitic basement
632   within the Cache Creek terrane; tectonic and metallogenic significance. *British
633   Columbia Geological Survey Field Report, 104N/12*.

634 Béchennec, F., Roger, J., Le Métour, J., & Wyns, R. (Cartographer). (1992). Geological Map
635   Oman 1 : 250.000, Seeb - Sheet NF40-03

636 Beinlich, A., Austrheim, H., Mavromatis, V., Grguric, B., Putnis, C. V., & Putnis, A. (2018).
637   Peridotite weathering is the missing ingredient of Earth's continental crust
638   composition. *Nature Communications, 9*(1), 634. doi:10.1038/s41467-018-03039-9

639 Beinlich, A., Plümper, O., Hövelmann, J., Austrheim, H., & Jamtveit, B. (2012). Massive
640   serpentinite carbonation at Linnajavri, N–Norway. *Terra Nova, 24*(6), 446-455.
641   doi:10.1111/j.1365-3121.2012.01083.x

642 Beinlich, A., Plümper, O., Boter, E., Müller, I. A., Kourim, F., Ziegler, M., . . . the Oman
643   Drilling Project Science Team. (2020). Ultramafic rock carbonation: Constraints
644   from listvenite core BT1B, Oman Drilling Project. *Journal of Geophysical Research:
645   Solid Earth, n/a*(n/a), e2019JB019060. doi:10.1029/2019JB019060

646 Billi, A. (2007). On the extent of size range and power law scaling for particles of natural
647   carbonate fault cores. *Journal of Structural Geology, 29*(9), 1512-1521.
648   doi:https://doi.org/10.1016/j.jsg.2007.06.007

649 Chavagnac, V., Monnin, C., Ceuleneer, G., Boulart, C., & Hoareau, G. (2013).
650   Characterization of hyperalkaline fluids produced by low-temperature
651   serpentinization of mantle peridotites in the Oman and Ligurian ophiolites.
652   *Geochemistry, geophysics, geosystems, 14*(7), 2496-2522. doi:10.1002/ggge.20147

653 Coleman, R. G. (1981). Tectonic setting for ophiolite obduction in Oman. *Journal of
654   Geophysical Research: Solid Earth, 86*(B4), 2497-2508.
655   doi:10.1029/JB086iB04p02497

656 Cowan, R. J., Searle, M. P., & Waters, D. J. (2014). Structure of the metamorphic sole to the
657   Oman Ophiolite, Sumeini Window and Wadi Tayyin: implications for ophiolite
658   obduction processes. *Geological Society, London, Special Publications, 392*(1), 155.
659   doi:10.1144/SP392.8

660 de Obeso, J. C., & Kelemen, P. B. (2018). Fluid rock interactions on residual mantle
661   peridotites overlain by shallow oceanic limestones: Insights from Wadi Fins,
662   Sultanate of Oman. *Chemical Geology, 498*, 139-149.
663   doi:https://doi.org/10.1016/j.chemgeo.2018.09.022

664 Escayola, M., Proenza, J., van Staal, C., Rogers, N., & Skulski, T. (2009). The Point Rousse
665   listvenites, Baie Verte, Newfoundland: altered ultramafic rocks with potential for
666   gold mineralization. *Current Research Geological Survey Report, 09-1*, 1-12.

667 Evans, O., Spiegelman, M., & Kelemen, P. B. (2020). Phase-Field Modeling of Reaction-
668   Driven Cracking: Determining Conditions for Extensive Olivine Serpentinization.
669   *Journal of Geophysical Research: Solid Earth, 125*(1), e2019JB018614.
670   doi:10.1029/2019JB018614

671 Falk, E. S., & Kelemen, P. B. (2015). Geochemistry and petrology of listvenite in the Samail
672   ophiolite, Sultanate of Oman: Complete carbonation of peridotite during ophiolite
673   emplacement. *Geochimica et Cosmochimica Acta, 160*, 70-90.
674   doi:10.1016/j.gca.2015.03.014

675 Farough, A., Moore, D. E., Lockner, D. A., & Lowell, R. P. (2016). Evolution of fracture
676   permeability of ultramafic rocks undergoing serpentinization at hydrothermal
677   conditions: An experimental study. *Geochemistry, geophysics, geosystems, 17*(1), 44-
678   55. doi:10.1002/2015GC005973

679 Ghent, E. D., & Stout, M. Z. (1981). Metamorphism at the base of the Samail Ophiolite,
680   southeastern Oman Mountains. *Journal of Geophysical Research: Solid Earth*,
681   86(B4), 2557-2571. doi:10.1029/JB086iB04p02557

682 Giampouras, M., Garrido, C. J., Bach, W., Los, C., Fussmann, D., Monien, P., & García-Ruiz,
683   J. M. (2020). On the controls of mineral assemblages and textures in alkaline springs,
684   Samail Ophiolite, Oman. *Chemical Geology, 533*, 119435.
685   doi:10.1016/j.chemgeo.2019.119435

686 Glennie, K. W., Boeuf, M. G. A., Clarke, M. W. H., Moody Stuart, M., Pilaar, W. F. H., &
687   Reinhardt, B. M. (1974). Geology of the Oman mountains. *Verhandelingen van het
688   Koninklink Nederlands Geologisch Mijnbouwkundig Genootschap, 31.*

689 Godard, M., Bennett, E., Carter, E., Kourim, F., Lafay, R., Noël, J., ... & Harris, M. (2017).
690   Geochemical and Mineralogical Profiles Across the Listvenite-Metamorphic
691   Transition in the Basal Megathrust of the Oman Ophiolite: First Results from
692   Drilling at Oman Drilling Project Hole BT1B. In *AGU Fall Meeting 2017, abstracts*
693   V24E-07.

694 Godard, M., Jousselin, D., & Bodinier, J.-L. (2000). Relationships between geochemistry and
695   structure beneath a palaeo-spreading centre: a study of the mantle section in the
696   Oman ophiolite. *Earth and Planetary Science Letters, 180*(1), 133-148.
697   doi:https://doi.org/10.1016/S0012-821X(00)00149-7

698 Godard, M., Luquot, L., Andreani, M., & Gouze, P. (2013). Incipient hydration of mantle
699   lithosphere at ridges: A reactive-percolation experiment. *Earth and Planetary
700   Science Letters, 371-372*, 92-102. doi:https://doi.org/10.1016/j.epsl.2013.03.052

701 Gomez-Rivas, E., Bons, P. D., Koehn, D., Urai, J. L., Arndt, M., Virgo, S., . . . Blum, P.
702   (2014). The Jabal Akhdar dome in the Oman Mountains: Evolution of a dynamic
703   fracture system. *American Journal of Science, 314*(7), 1104-1139.

704 Grobe, A., Urai, J. L., Littke, R., & Lünsdorf, N. K. (2016). Hydrocarbon generation and
705   migration under a large overthrust: The carbonate platform under the Semail

706 Ophiolite, Jebel Akhdar, Oman. *International Journal of Coal Geology, 168*, 3-19.
707 doi:https://doi.org/10.1016/j.coal.2016.02.007

708 Grobe, A., Virgo, S., von Hagke, C., Urai, J. L., & Littke, R. (2018). Multiphase Structural
709 Evolution of a Continental Margin During Obduction Orogeny: Insights From the
710 Jebel Akhdar Dome, Oman Mountains. *Tectonics, 37*(3), 888-913.
711 doi:10.1002/2016TC004442

712 Grobe, A., von Hagke, C., Littke, R., Dunkl, I., Wübbeler, F., Muchez, P., & Urai, J. L.
713 (2019). Tectono-thermal evolution of Oman's Mesozoic passive continental margin
714 under the obducting Semail Ophiolite: a case study of Jebel Akhdar, Oman. *Solid*
715 *Earth, 10*(1), 149-175. doi:10.5194/se-10-149-2019

716 Guilmette, C., Smit, M. A., van Hinsbergen, D. J. J., Gürer, D., Corfu, F., Charette, B., . . .
717 Savard, D. (2018). Forced subduction initiation recorded in the sole and crust of the
718 Semail Ophiolite of Oman. *Nature Geoscience, 11*(9), 688-695. doi:10.1038/s41561-
719 018-0209-2

720 Hacker, B. R., & Mosenfelder, J. L. (1996). Metamorphism and deformation along the
721 emplacement thrust of the Samail ophiolite, Oman. *Earth and Planetary Science*
722 *Letters, 144*(3), 435-451. doi:https://doi.org/10.1016/S0012-821X(96)00186-0

723 Hacker, B. R., Mosenfelder, J. L., & Gnos, E. (1996). Rapid emplacement of the Oman
724 ophiolite: Thermal and geochronologic constraints. *Tectonics, 15*(6), 1230-1247.
725 doi:10.1029/96TC01973

726 Halls, C., & Zhao, R. (1995). Listvenite and related rocks: perspectives on terminology and
727 mineralogy with reference to an occurrence at Cregganbaun, Co. Mayo, Republic of
728 Ireland. *Mineralium Deposita, 30*(3-4), 303-313. doi:10.1007/bf00196366

729 Hanghøj, K., Kelemen, P. B., Hassler, D., & Godard, M. (2010). Composition and Genesis of
730 Depleted Mantle Peridotites from the Wadi Tayin Massif, Oman Ophiolite; Major
731 and Trace Element Geochemistry, and Os Isotope and PGE Systematics. *Journal of*
732 *Petrology, 51*(1-2), 201-227. doi:10.1093/petrology/egp077

733 Hansen, L. D., Dipple, G. M., Gordon, T. M., & Kellett, D. A. (2005). Carbonated
734 serpentinite (listwanite) at Atlin, British Columbia: A geological analogue to carbon
735 dioxide sequestration. *Canadian Mineralogist, 43*(1), 225-239.

736 Hansman, R. J., Albert, R., Gerdes, A., & Ring, U. (2018). Absolute ages of multiple
737 generations of brittle structures by U-Pb dating of calcite. *Geology, 46*(3), 207-210.
738 doi:10.1130/G39822.1

739 Hansman, R. J., Ring, U., Thomson, S. N., den Brok, B., & Stübner, K. (2017). Late Eocene
740 Uplift of the Al Hajar Mountains, Oman, Supported by Stratigraphy and Low-
741 Temperature Thermochronology. *Tectonics, 36*(12), 3081-3109.
742 doi:10.1002/2017TC004672

743 Holyoke, C. W., Kronenberg, A. K., Newman, J., & Ulrich, C. (2014). Rheology of
744 magnesite. *Journal of Geophysical Research: Solid Earth, 119*(8), 6534-6557.
745 doi:10.1002/2013JB010541

746 Hopson, C. A., Coleman, R. G., Gregory, R. T., Pallister, J. S., & Bailey, E. H. (1981).
747   Geologic section through the Samail Ophiolite and associated rocks along a Muscat-
748   Ibra Transect, southeastern Oman Mountains. *Journal of Geophysical Research:*
749   *Solid Earth, 86*(B4), 2527-2544. doi:10.1029/JB086iB04p02527

750 Hövelmann, J., Austrheim, H., & Jamtveit, B. (2013). Microstructure and porosity evolution
751   during experimental carbonation of a natural peridotite. *Chemical Geology, 334*, 254-
752   265. doi:10.1016/j.chemgeo.2012.10.025

753 Huang, J., Hao, J., Huang, F., & Sverjensky, D. A. (2019). Mobility of chromium in high
754   temperature crustal and upper mantle fluids. *Geochemical Perspectives Letters, 12*,
755   1-6. doi:http://dx.doi.org/10.7185/geochemlet.1926

756 Hyndman, R. D., & Peacock, S. M. (2003). Serpentinization of the forearc mantle. *Earth and*
757   *Planetary Science Letters, 212*(3-4), 417-432. doi:10.1016/s0012-821x(03)00263-2

758 Jacobs, J., Thomas, R. J., Ksienzyk, A. K., & Dunkl, I. (2015). Tracking the Oman Ophiolite
759   to the surface — New fission track and (U–Th)/He data from the Aswad and Khor
760   Fakkan Blocks, United Arab Emirates. *Tectonophysics, 644-645*, 68-80.
761   doi:https://doi.org/10.1016/j.tecto.2014.12.018

762 Jöns, N., & Bach, W. (2013). Serpentinization. In J. Harff, M. Meschede, S. Petersen, & J.
763   Thiede (Eds.), *Encyclopedia of Marine Geosciences* (pp. 1-12). Dordrecht: Springer
764   Netherlands.

765 Kelemen, P. B., Aines, R., Bennett, E., Benson, S. M., Carter, E., Coggon, J. A., . . . Wilcox,
766   J. (2018). In situ carbon mineralization in ultramafic rocks: Natural processes and
767   possible engineered methods. *Energy Procedia, 146*, 92-102.
768   doi:https://doi.org/10.1016/j.egypro.2018.07.013

769 Kelemen, P., Godard, M., Johnson, K. T. M., Okazaki, K., Manning, C. E., Urai, J. L., . . . and
770   the Oman Drilling Project Phase I Science Party. (2017). Peridotite carbonation at the
771   leading edge of the mantle wedge: OmDP Site BT1. *AGU Fall meeting*, abstract
772   V24E-06.

773 Kelemen, P. B., & Hirth, G. (2012). Reaction-driven cracking during retrograde
774   metamorphism: Olivine hydration and carbonation. *Earth and Planetary Science*
775   *Letters, 345-348*(Supplement C), 81-89.
776   doi:https://doi.org/10.1016/j.epsl.2012.06.018

777 Kelemen, P. B., & Manning, C. E. (2015). Reevaluating carbon fluxes in subduction zones,
778   what goes down, mostly comes up. *Proceedings of the National Academy of*
779   *Sciences, 112*(30), E3997-4006. doi:10.1073/pnas.1507889112

780 Kelemen, P. B., & Matter, J. (2008). In situ carbonation of peridotite for CO_2 storage.
781   *Proceedings of the National Academy of Sciences, 105*(45), 17295-17300.

782 Kelemen, P. B., Matter, J., Streit, E. E., Rudge, J. F., Curry, W. B., & Blusztajn, J. (2011).
783   Rates and Mechanisms of Mineral Carbonation in Peridotite: Natural Processes and
784   Recipes for Enhanced, in situ CO_2 Capture and Storage. In R. Jeanloz & K. H.

Freeman (Eds.), *Annual Review of Earth and Planetary Sciences, Vol 39* (Vol. 39, pp. 545-576).

Kelemen, P.B., Matter, J.M., Teagle, D.A.H., Coggon, J.A., and the Oman Drilling Project Science Team. (2020). *Proceedings of the Oman Drilling Project:* College Station, TX (International Ocean Discovery Program). https://doi.org/10.14379/OmanDP.proc.2020

Keulen, N., Stünitz, H., & Heilbronner, R. (2008). Healing microstructures of experimental and natural fault gouge. *Journal of Geophysical Research: Solid Earth, 113*(B6). doi:10.1029/2007JB005039

Klein, F., & Garrido, C. J. (2011). Thermodynamic constraints on mineral carbonation of serpentinized peridotite. *Lithos, 126*(3-4), 147-160. doi:10.1016/j.lithos.2011.07.020

Klein, F., Grozeva, N. G., Seewald, J. S., McCollom, T. M., Humphris, S. E., Moskowitz, B., . . . Kahl, W.-A. (2015). Experimental constraints on fluid-rock reactions during incipient serpentinization of harzburgite. *American Mineralogist, 100*(4), 991-1002. doi:10.2138/am-2015-5112

Lacinska, A. M., & Styles, M. T. (2012). Silicified serpentinite – a residuum of a Tertiary palaeo-weathering surface in the United Arab Emirates. *Geological Magazine, 150*(3), 385-395. doi:10.1017/S0016756812000325

Lafay, R., Godard, M., Menzel, M., Beinlich, A., Kourim, F., Decrausaz, T., and the Oman Drilling Project Phase 1 Science Party. Listvenization processes in the mantle atop the Samail ophiolite metamorphic sole: Mineralogical and thermodynamic constraints. *Proceedings of the International Conference on Ophiolites and Oceanic Lithosphere*, 12-14 January, Sultan Qaboos University, Oman, 2020, page 129.

Laurich, B., Urai, J. L., Vollmer, C., & Nussbaum, C. (2018). Deformation mechanisms and evolution of the microstructure of gouge in the Main Fault in Opalinus Clay in the Mont Terri rock laboratory (CH). *Solid Earth, 9*(1), 1-24. doi:10.5194/se-9-1-2018

Li, J., & Hitch, M. (2018). Mechanical activation of magnesium silicates for mineral carbonation, a review. *Minerals Engineering, 128*, 69-83. doi:https://doi.org/10.1016/j.mineng.2018.08.034

Lisabeth, H. P., Zhu, W., Kelemen, P. B., & Ilgen, A. (2017). Experimental evidence for chemo-mechanical coupling during carbon mineralization in ultramafic rocks. *Earth and Planetary Science Letters, 474*(Supplement C), 355-367. doi:https://doi.org/10.1016/j.epsl.2017.06.045

Macdonald, A. H., & Fyfe, W. S. (1985). Rate of serpentinization in seafloor environments. *Tectonophysics, 116*(1), 123-135. doi:https://doi.org/10.1016/0040-1951(85)90225-2

Malthe-Sørenssen, A., Jamtveit, B., & Meakin, P. (2006). Fracture Patterns Generated by Diffusion Controlled Volume Changing Reactions. *Physical Review Letters, 96*(24), 245501. doi:10.1103/PhysRevLett.96.245501

823 Manning, C. E., Kelemen, P. B., Michibayashi, K., Harris, M., Urai, J. L., de Obeso, J. C., . . .
824   and the Oman Drilling Project Phase 1 Science Party. (2017). Transformation of
825   Serpentinite to Listvenite as Recorded in the Vein History of Rocks From Oman
826   Drilling Project Hole BT1B. *AGU Fall Meeting Abstract, V24E-08.*

827 Malvoisin, B., Auzande, A.L., Kelemen, P.B., and the Oman Drilling Project Science Party.
828   (2020). The mechanism of fluid pathway preservation during solid volume increase
829   in serpentinization. *Geology*, submitted April 2020

830 Menzel, M. D., Garrido, C. J., López Sánchez-Vizcaíno, V., Marchesi, C., Hidas, K.,
831   Escayola, M. P., & Delgado Huertas, A. (2018). Carbonation of mantle peridotite by
832   CO_2-rich fluids: the formation of listvenites in the Advocate ophiolite complex
833   (Newfoundland, Canada). *Lithos, 323*, 238-261. doi:10.1016/j.lithos.2018.06.001

834 Miller, J. M., Gregory, R. T., Gray, D. R., & Foster, D. A. (1999). Geological and
835   geochronological constraints on the exhumation of a high-pressure metamorphic
836   terrane, Oman. *Geological Society, London, Special Publications, 154*(1), 241.
837   doi:10.1144/GSL.SP.1999.154.01.11

838 Monnier, C., Girardeau, J., Le Mée, L., & Polvé, M. (2006). Along-ridge petrological
839   segmentation of the mantle in the Oman ophiolite. *Geochemistry, geophysics,
840   geosystems, 7*(11). doi:10.1029/2006GC001320

841 Nasir, S., Al Sayigh, A. R., Al Harthy, A., Al-Khirbash, S., Al-Jaaidi, O., Musllam, A., . . .
842   Al-Bu'saidi, S. (2007). Mineralogical and geochemical characterization of listwaenite
843   from the Semail Ophiolite, Oman. *Geochemistry, 67*(3), 213-228.
844   doi:10.1016/j.chemer.2005.01.003

845 Nicolas, A., & Boudier, F. (1995). Mapping oceanic ridge segments in Oman ophiolite.
846   *Journal of Geophysical Research: Solid Earth, 100*(B4), 6179-6197.
847   doi:10.1029/94JB01188

848 Nicolas, A., Boudier, F., & Ildefonse, B. (1996). Variable crustal thickness in the Oman
849   ophiolite: Implication for oceanic crust. *Journal of Geophysical Research: Solid
850   Earth, 101*(B8), 17941-17950. doi:10.1029/96JB00195

851 Noël, J., Godard, M., Oliot, E., Martinez, I., Williams, M., Boudier, F., . . . Gouze, P. (2018).
852   Evidence of polygenetic carbon trapping in the Oman Ophiolite: Petro-structural,
853   geochemical, and carbon and oxygen isotope study of the Wadi Dima harzburgite-
854   hosted carbonates (Wadi Tayin massif, Sultanate of Oman). *Lithos*.
855   doi:https://doi.org/10.1016/j.lithos.2018.08.020

856 Nolan, S. C., Skelton, P. W., Clissold, B. P., & Smewing, J. D. (1990). Maastrichtian to early
857   Tertiary stratigraphy and palaeogeography of the Central and Northern Oman
858   Mountains. *Geological Society, London, Special Publications, 49*(1), 495.
859   doi:10.1144/GSL.SP.1992.049.01.31

860 Oelkers, E. H., Declercq, J., Saldi, G. D., Gislason, S. R., & Schott, J. (2018). Olivine
861   dissolution rates: A critical review. *Chemical Geology, 500*, 1-19.
862   doi:https://doi.org/10.1016/j.chemgeo.2018.10.008

863 Pachana, K., Zuddas, P., & Censi, P. (2012). Influence of pH and temperature on the early
864   stage of mica alteration. *Applied Geochemistry, 27*(9), 1738-1744.
865   doi:https://doi.org/10.1016/j.apgeochem.2012.02.009

866 Passchier, C. W., & Trouw, R. A. J. (2005). *Microtectonics* (2nd ed.). Berlin Heidelberg New
867   York: Springer.

868 Paukert, A. N., Matter, J. M., Kelemen, P. B., Shock, E. L., & Havig, J. R. (2012). Reaction
869   path modeling of enhanced in situ CO2 mineralization for carbon sequestration in the
870   peridotite of the Samail Ophiolite, Sultanate of Oman. *Chemical Geology, 330-331*,
871   86-100. doi:https://doi.org/10.1016/j.chemgeo.2012.08.013

872 Peuble, S., Andreani, M., Godard, M., Gouze, P., Barou, F., Van de Moortele, B., . . .
873   Reynard, B. (2015). Carbonate mineralization in percolated olivine aggregates:
874   Linking effects of crystallographic orientation and fluid flow. *American*
875   *Mineralogist, 100*(2-3), 474-482. doi:10.2138/am-2015-4913

876 Peuble, S., Andreani, M., Gouze, P., Pollet-Villard, M., Reynard, B., & Van de Moortele, B.
877   (2018). Multi-scale characterization of the incipient carbonation of peridotite.
878   *Chemical Geology, 476*(Supplement C), 150-160.
879   doi:https://doi.org/10.1016/j.chemgeo.2017.11.013

880 Plümper, O., Røyne, A., Magrasó, A., & Jamtveit, B. (2012). The interface-scale mechanism
881   of reaction-induced fracturing during serpentinization. *Geology, 40*(12), 1103-1106.
882   doi:10.1130/G33390.1

883 Qiu, T., & Zhu, Y. (2018). Listwaenite in the Sartohay ophiolitic mélange (Xinjiang, China):
884   A genetic model based on petrology, U-Pb chronology and trace element
885   geochemistry. *Lithos, 302-303*, 427-446. doi:10.1016/j.lithos.2018.01.029

886 Rai, D., Sass, B. M., & Moore, D. A. (1987). Chromium(III) hydrolysis constants and
887   solubility of chromium(III) hydroxide. *Inorganic Chemistry, 26*(3), 345-349.
888   doi:10.1021/ic00250a002

889 Rajendran, S., Nasir, S., Kusky, T. M., Ghulam, A., Gabr, S., & El-Ghali, M. A. K. (2013).
890   Detection of hydrothermal mineralized zones associated with listwaenites in Central
891   Oman using ASTER data. *Ore Geology Reviews, 53*, 470-488.
892   doi:https://doi.org/10.1016/j.oregeorev.2013.02.008

893 Rioux, M., Bowring, S., Kelemen, P., Gordon, S., Miller, R., & Dudás, F. (2013). Tectonic
894   development of the Samail ophiolite: High-precision U-Pb zircon geochronology and
895   Sm-Nd isotopic constraints on crustal growth and emplacement. *Journal of*
896   *Geophysical Research: Solid Earth, 118*(5), 2085-2101. doi:10.1002/jgrb.50139

897 Rudge, J. F., Kelemen, P. B., & Spiegelman, M. (2010). A simple model of reaction-induced
898   cracking applied to serpentinization and carbonation of peridotite. *Earth and*
899   *Planetary Science Letters, 291*(1), 215-227.
900   doi:https://doi.org/10.1016/j.epsl.2010.01.016

901 Saddiqi, O., Michard, A., Goffe, B., Poupeau, G. r., & Oberhänsli, R. (2006). Fission-track
902   thermochronology of the Oman Mountains continental windows, and current

903   problems of tectonic interpretation. *Bulletin de la Société Géologique de France,*
904   *177*(3), 127-134. doi:10.2113/gssgfbull.177.3.127

905   Scharf, A., Mattern, F., Bolhar, R., Bailey, C. M., Ring, U. (2020). U-Pb dating of
906   postobductional carbonate veins in listwaenite of the Oman Mountains near Fanja. .
907   *Proceedings of the International Conference on Ophiolites and Oceanic Lithosphere,*
908   12-14th January, 2020, Sultan Qaboos University, Muscat, Sultanate of Oman, page
909   220.

910   Scharf, A., Mattern, F., Moraetis, D., Callegari, I., & Weidle, C. (2019). Postobductional
911   Kinematic Evolution and Geomorphology of a Major Regional Structure—The
912   Semail Gap Fault Zone (Oman Mountains). *Tectonics, 38*(8), 2756-2778.
913   doi:10.1029/2019TC005588

914   Searle, M., & Cox, J. (1999). Tectonic setting, origin, and obduction of the Oman ophiolite.
915   *GSA Bulletin, 111*(1), 104-122. doi:10.1130/0016-
916   7606(1999)111<0104:TSOAOO>2.3.CO;2

917   Searle, M. P., Waters, D. J., Martin, H. N., & Rex, D. C. (1994). Structure and metamorphism
918   of blueschist–eclogite facies rocks from the northeastern Oman Mountains. *Journal*
919   *of the Geological Society, 151*(3), 555. doi:10.1144/gsjgs.151.3.0555

920   Soret, M., Agard, P., Dubacq, B., Plunder, A., & Yamato, P. (2017). Petrological evidence for
921   stepwise accretion of metamorphic soles during subduction infancy (Semail
922   ophiolite, Oman and UAE). *Journal of Metamorphic Geology, 35*(9), 1051-1080.
923   doi:10.1111/jmg.12267

924   Soret, M., Bonnet, G., Larson, K., Agard, P., Cottle, J., Dubacq, B., Button, M. Slow
925   subduction initiation forces fast ophiolite formation. *Proceedings of the International*
926   *Conference on Ophiolites and the Oceanic Lithosphere: Results of the Oman Drilling*
927   *Project and Related Research* 12-14th January, 2020, Sultan Qaboos University,
928   Muscat, Sultanate of Oman, page 234.

929   Stanger, G. (1985). Silicified serpentinite in the Semail nappe of Oman. *Lithos, 18*, 13-22.
930   doi:https://doi.org/10.1016/0024-4937(85)90003-9

931   Streit, E., Kelemen, P., & Eiler, J. (2012). Coexisting serpentine and quartz from carbonate-
932   bearing serpentinized peridotite in the Samail Ophiolite, Oman. *Contributions to*
933   *Mineralogy and Petrology, 164*(5), 821-837. doi:10.1007/s00410-012-0775-z

934   Tutolo, B. M., Mildner, D. F. R., Gagnon, C. V. L., Saar, M. O., & Seyfried, W. E., Jr.
935   (2016). Nanoscale constraints on porosity generation and fluid flow during
936   serpentinization. *Geology, 44*(2), 103-106. doi:10.1130/G37349.1

937   Ulven, O. I., Storheim, H., Austrheim, H., & Malthe-Sørenssen, A. (2014). Fracture initiation
938   during volume increasing reactions in rocks and applications for CO2 sequestration.
939   *Earth and Planetary Science Letters, 389*, 132-142. doi:10.1016/j.epsl.2013.12.039

940   van Noort, R., Wolterbeek, T. K. T., Drury, M. R., Kandianis, M. T., & Spiers, C. J. (2017).
941   The force of crystallization and fracture propagation during in-situ carbonation of
942   peridotite. *Minerals, 7*(10). doi:10.3390/min7100190

943 Villey. M., Le Métour J. & de Gramont, X. (1986). Geological Map of Fanjah. Bureau de
944   Recherches Géologiques et Minières (BRGM), Orléans, France; Muscat, Oman,
945   Ministry of Petroleum and Minerals, Directorate General of Minerals, Sultanate of
946   Oman.

947 Virgo, S., Arndt, M., Sobisch, Z., & Urai, J. L. (2013). Development of fault and vein
948   networks in a carbonate sequence near Hayl al-Shaz, Oman Mountains. *GeoArabia,*
949   *18*(2), 99-136.

950 Virgo, S., Heup, T., Urai, J. L., & Berlageet. T, (2016). Virtual Petrography (ViP) – A virtual
951   microscope for the geosciences. *Geophysical Research Abstracts,* 18, EGU2016-
952   14669-1 http://meetingorganizer.copernicus.org/EGU2016/EGU2016-14669-1.pdf

953 Wilde, A., Simpson, L., & Hanna, S. (2002) Preliminary study of Cenozoic hydrothermal
954   alteration and platinum deposition in the Oman Ophiolite. *Vol. 6. Journal of the*
955   *Virtual Explorer 6* (pp. 7-13).

956 Xing, T., Zhu, W., Fusseis, F., & Lisabeth, H. (2018). Generating porosity during olivine
957   carbonation via dissolution channels and expansion cracks. *Solid Earth, 9*(4), 879-
958   896. doi:10.5194/se-9-879-2018Zheng, X., Cordonnier, B., Zhu, W., Renard, F., &
959   Jamtveit, B. (2018). Effects of Confinement on Reaction-Induced Fracturing During
960   Hydration of Periclase. *Geochemistry, geophysics, geosystems, 19*(8), 2661-2672.
961   doi:10.1029/2017GC007322

962 Zhu, W., Fusseis, F., Lisabeth, H., Xing, T., Xiao, X., De Andrade, V., & Karato, S.-i. (2016).
963   Experimental evidence of reaction-induced fracturing during olivine carbonation.
964   Geophysical Research Letters, 43(18), 9535-9543. doi:10.1002/2016GL070834

965

Supplementary Table S1: Overview of studied thin sections of samples with cataclastic structures in Oman Drilling Project Hole BT1B

Sample ID (exp. 5057_4B)	Lithology comment	Depth (m)	ViP	SEM
BT1B_7-2_76-79	localized cataclasite in red listvenite *#	7.66	x	x
BT1B_8-2_2-4	dolomite-cemented listvenite breccia with cataclasite fragments*#	9.57		
BT1B_9-3_28-31	grey cataclastic listvenite *#	13.70	x	x
BT1B_11-2_31-34	localized cataclasite in grey listvenite *#	17.53		
BT1B_13-3_62-64	localized cataclasite in listvenite *#	23.46	x	x
BT1B_17-2_55-60	red cataclastic listvenite and sharp fault *	31.38	x	x
BT1B_18-2_60-63	localized cataclasite in red listvenite *#	34.67		
BT1B_18-3_16-19	localized cataclasite in orange listvenite *#	35.22	x	x
BT1B_40-3_4-7	localized cataclasite in ophicarbonate	86.97	x	
BT1B_48-1_32-37	localized cataclasite in veined listvenite #	109.67	x	
BT1B_51-4_20-25	localized cataclasite in veined listvenite #	118.08		
BT1B_53-2_19-24	localized µm-scale cataclasite in listvenite	122.34		
BT1B_53-3_17-22	localized µm-scale cataclasites in listvenite #	123.10		
BT1B_54-2_27-32	localized µm-scale cataclasites in listvenite #	125.69		
BT1B_54-3_42-47	localized cataclasite in listvenite #	126.62		
BT1B_58-3_20-25	Localized cataclasite in listvenite *#	135.68		
BT1B_63-3_61-66	localized cataclasite in fuchsite-rich listvenite #	151.43	x	
BT1B_65-2_22-26	localized cataclasite in grey listvenite *	156.17	x	x
BT1B_66-2_11-16	cataclastic listvenite in listvenite *#	159.14	x	
BT1B_66-2_78-83	localized cataclasite in listvenite #	159.81	x	
BT1B_67-2_36-40	dolomite-cemented breccia in fuchsite-listvenite	162.11	x	x
BT1B_70-3_55-60	localized cataclasite in grey massive listvenite *#	172.25		
BT1B_71-2_21-26	white-green cataclasite in foliated listvenite *#	174.27	x	
BT1B_75-3_36-41	cataclastic listvenite with dark matrix*	187.40		
BT1B_76-1_42-48	grey cataclastic listvenite *#	188.87		
BT1B_78-2_34-38	localized µm-scale cataclasite cutting foliated dolomite listvenite #	195.87	x	x
BT1B_100-2_32-35	cataclastic metamorphic sole	244.62	x	x

Microstructural evidence for cataclasis post-dating listvenite formation in thin sections:

* cataclasite contains clearly identifiable rotated clasts of listvenite and vein fragments

cataclasite truncates veins that otherwise crosscut listvenite